Correcting Motion Artifacts in Multi-Shot Diffusion-Weighted EPI Using Iterative Phase Cycling

by

Shayan Guhaniyogi

Department of Biomedical Engineering
Duke University

Date: _____

Approved:

_____
Allen W. Song, Supervisor

_____
Chunlei Liu

_____
Nan-Kuei Chen

Thesis submitted in partial fulfillment of the requirements for the degree of
Master of Science in the Department of Biomedical Engineering
in the Graduate School of Duke University
2012

Abstract

Correcting Motion Artifacts in Multi-Shot Diffusion-Weighted EPI Using Iterative Phase Cycling

by

Shayan Guhaniyogi

Department of Biomedical Engineering
Duke University

Date: _____

Approved:

_____
Allen W. Song, Supervisor

_____
Chunlei Liu

_____
Nan-Kuei Chen

An abstract of a thesis submitted in partial fulfillment of the requirements for the degree of Master of Science in the Department of Biomedical Engineering in the Graduate School of Duke University
2012

Copyright © 2012 by Shayan Guhaniyogi
All rights reserved except the rights granted by the
Creative Commons Attribution-Noncommercial Licence

Abstract

Diffusion-weighted MRI (DWI) is an essential tool in clinical applications such as detecting ischemic stroke, and in research applications studying neuronal connectivity in the brain. Diffusion-weighted imaging with multi-shot echo-planar acquisition (DWEPI) offers several advantages over single-shot EPI, including improved spatial resolution and reduced off-resonance and susceptibility artifacts. However a major limitation of multi-shot DWEPI is its sensitivity to patient motion during the application of diffusion gradients; the motion generates phase errors which vary from shot to shot, resulting in artifacts in the reconstructed image.

Most current methods for correcting motion-induced artifacts involve the use of navigator echoes to estimate the shot-to-shot phase errors. Accurate navigator information comes at the expense of increased scan times however, which is generally undesirable. The aim of this study is to therefore develop and demonstrate the use of an alternative phase estimation technique, iterative phase-cycling, as a new method to correct motion artifacts in DWI without the use of navigators. The developed method involves an iterative column by column estimation of phase errors in the aliased image and reconstruction of an artifact free image using the estimated errors.

In this study the technique was applied to correct artifacts in simulated images, hybrid-simulated images, and true four-shot DWEPI images. Accuracy of the phase-cycling method was evaluated by computing residual image errors and ghost-to-noise ratios after correction. The efficiency of phase-cycling was evaluated by recording

computation times of the correction process. Multiple optimization techniques were developed and used in the experiments, and the accuracy/efficiency of these techniques were also assessed.

Results of the experiments demonstrated the ability of phase-cycling to greatly reduce motion-induced artifacts in multi-shot DWEPI at reasonable computation times. The phase-cycling model used in this study accurately estimated linear and nonlinear errors along the frequency encoding direction and linear errors along the phase encoding direction. An additional mathematical framework is presented illustrating the potential of phase-cycling to correct nonlinear errors along the phase encoding direction in future work.

The study establishes the developed technique as a unique and effective method for correcting motion artifacts in DWEPI without the cost of increased scan times.

Contents

List of Tables

List of Figures

1

Introduction

Within the past two decades diffusion-weighted MRI (DWI) has become established as an important diagnostic tool in both clinical and research settings. One of its greatest clinical utilities is in the assessment of acute ischemic stroke in its early stages. DWI has been shown to be sensitive to changes in proton diffusion due to stroke within minutes after the cessation of blood flow [1, 2]. The early diagnosis of acute stroke allows for greater flexibility in treatment options, and can greatly improve the therapeutic outcome for patients [3, 4]. As a result DWI is of great value for early stroke diagnosis and treatment. In addition, DWI is also capable of sucessfully discriminating among abnormalities such as brain tumors and abscesses [5, 6] in diagnostic applications. In research settings diffusion-tensor imaging (DTI), the extension of DWI, can be used for mapping neuronal connectivity in the brain [7–10]. This technique has shown promise for characterizing the anatomical basis of neurodegenerative disorders such as Parkinson's and Alzheimer's [9, 10].

In spite of the impressive and growing number of uses of DWI, it continues to be limited by its sensitivity to patient motion. The large diffusion gradients used in DWI make the technique sensitive not only to proton movement via diffusion, but

also to patient movement. Such large-scale movement introduces distortions known as motion artifacts in DWI images, which degrade image quality and prevent proper visualization of anatomy. The most straightforward solution is to use mechanical restraints to restrict patient motion, however these are uncomfortable for the patient and are generally not effective [4].

The solution most common in clinical practice is to use a single-shot imaging technique such as echo-planar imaging (EPI). Single-shot EPI rapidly acquires the entirety of k-space with a single excitation, with typical acqusition times ranging on the order of tens of milliseconds. This fast acquisition essentially "freezes" the effects of patient motion, thereby creating images free of motion artifacts. There are however several drawbacks to using single-shot EPI [11–14]. Since all data is acquired with only one RF excitation, the maximum attainable spatial resolution is limited by T_2^* signal decay. Additionally, the long gradient-echo train length used in single-shot EPI reduces the signal-to-noise ratio (SNR) of images, and makes them vulnerable to a number of artifacts. These include artifacts arising from off-resonance effects, such as $\vec{B_0}$ field inhomogeneity, and from variations in magnetic susceptibility at air-tissue interfaces.

In order to overcome the limitations of single-shot techniques, multi-shot sequences such as multi-shot EPI are often used. In multi-shot EPI k-space data are acquired in multiple excitations, allowing higher attainable spatial resolutions, improved SNR, and reduced vulnerability to off-resonance and susceptibility artifacts. However, because of the multiple excitations used to acquire data, multi-shot EPI combined with DWI (DWEPI) is sensitive to patient motion during the application of diffusion gradients. Motion corrupts the data from each excitation differently, producing phase errors and k-space shifts which vary from shot-to-shot. This results in image artifacts when the corrupted data is reconstructed.

Correcting motion artifacts in multi-shot DWEPI is an area of ongoing research.

Various methods have been developed which retrospectively remove the artifacts using estimations of the motion-induced phase errors and k-space shifts. The majority of these methods employ the use of navigator echoes to estimate the phase and shift errors [11, 13, 15–19]. The major drawback in navigator-based estimation is the trade-off between accuracy and scan efficiency: low-resolution navigators may not accurately estimate errors, but more accurate high-resolution navigators come at the cost of increased scan times.

To avoid this trade-off of navigator correction, this study proposes an alternative phase estimation and artifact correction technique known as phase-cycling which does not require the use of navigators. The intention is to develop and implement an algorithm which iteratively estimates the motion-induced errors in multi-shot DWEPI, and thus has the ability to correct artifacts without affecting scan times.

2

Motion Artifacts and Correction

2.1 Motion Effects in DWI

The inherent purpose of DWI is to make acquired signals sensitive to molecular motion via diffusion, resulting in diffusion-weighted contrast. However this sensitivity to small molecular motion means that the signal will also be sensitive to large-scale motion resulting from patient movement. This is the primary technical difficulty in multi-shot DWI, and is a result of bulk motion during the large diffusion gradients applied at the beginning of a DWI sequence. Bulk motion can be characterized by both translation and rotation along/about any of the coordinate axes, and causes a corruption in the acquired signal given by [20]:

$$S_m(\vec{k}) = S_s(\vec{k} + \Delta\vec{k})e^{i\phi} \tag{2.1}$$

where $S_m(\vec{k})$ is the corrupted acquired data and $S_s(\vec{k})$ represents the ideal data. It can be seen from (2.1) that the corrupted data is characterized by a k-space shift $\Delta\vec{k}$ and phase offset ϕ of the ideal data.

The phase offset ϕ is from translational motion and is given by:

$$\phi = \gamma \int \vec{G}_d(t) \cdot \vec{T}(t) dt \tag{2.2}$$

where $\vec{G}_d(t)$ represents the diffusion gradient directions and magnitudes, and $\vec{T}(t)$ is the object translation vector.

The k-space shift $\Delta\vec{k}$ in (2.1) is due to rotational motion and is given by:

$$\Delta\vec{k} = \frac{\gamma}{2\pi} \int \vec{G}_d(t) \times \vec{\Theta}(t) dt \tag{2.3}$$

where $\vec{\Theta}(t)$ is the rotation vector that points in the direction of the rotation axis and has magnitude equal to the rotation angle in radians. By Fourier transform properties, the global phase offset and shift in the k-space domain correspond to a global phase offset and linear phase ramp, respectively, in image space. In other words, translational motion results in 0^{th} order phase errors and rotation results in 1^{st} order phase errors when considering the image domain.

Because bulk motion will typically vary from shot-to-shot in multi-shot acquisitions the data acquired in each shot will be perturbed differently. Therefore each set of data will acquire different phase offsets and k-space shifts. This is depicted in Fig. 2.1 (from [4]), which illustrates ideal (left column) and corrupted (right column) multi-shot DWEPI data and the resulting images reconstructed from each data set. It can be seen that the corrupted data due to motion results in severe motion artifacts in the image.

2.2 Correction Techniques

If the relative phase offsets and k-space shifts between shots or the corresponding 0^{th} and 1^{st} phase errors in the image domain can be estimated, it is possible to correct the data and reconstruct an image with reduced artifact. The current techniques

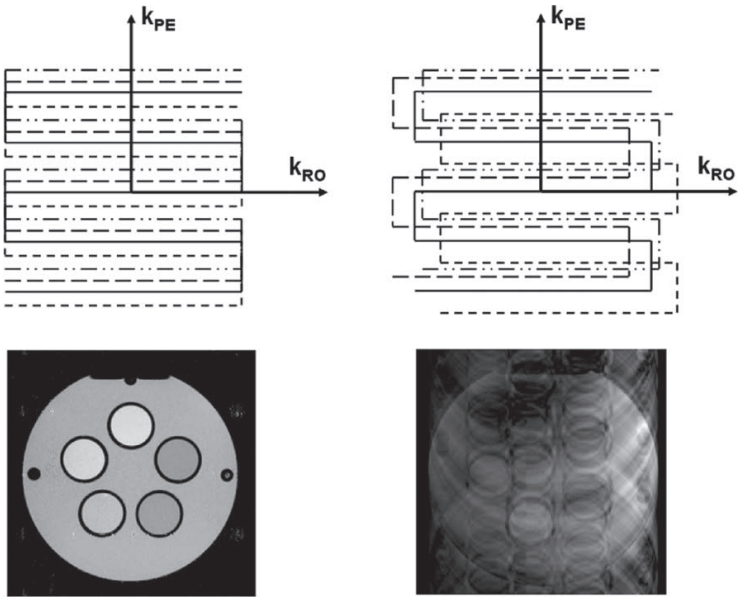

FIGURE 2.1: Example of motion-induced errors in multi-shot DWEPI [4]. (Left) Ideal data and an artifact-free image when no motion is present. (Right) Corrupted data in which k-space trajectories of each shot are shifted due to motion, and the resulting image with artifacts.

to accomplish this use either the incorporation of navigator echoes, or involve an iterative estimation procedure.

2.2.1 Navigator Echoes

Navigator echoes are partially acquired k-space data collected at either the beginning or end of a pulse sequence [20]. In multi-shot DWEPI, navigator echoes are collected for each shot in the same region of k-space (typically the center). Any motion effects in the image data for a particular shot will also be present in the navigator data. Therefore by comparing the differences in navigator data for each shot it is possible to estimate the phase and shift errors arising from motion.

Initial implementations used 1D navigation in a conventional spin-echo DWI sequence, acquiring a single navigator echo along the frequency encoding direction at each phase encoding step [15, 21]. Correction was done in image space by applying a

1D Fourier transform to the navigators to obtain a phase projection for each phase encoding step. The phase difference between a reference projection and all other projections is calculated, resulting in a phase correction map which is then used to correct the image data. The major limitations of these 1D navigation methods is that they can only for correct for errors in one direction [15, 21], and they are only reliable when a single diffusion gradient is applied in one direction [11, 15, 21]. Because motion typically affects multiple axes, and because diffusion gradients applied along multiple directions is necessary for high quality ADC maps [11, 16, 22], improved navigation techniques are required.

2D navigators acquire data over a two-dimensional region around the center of k-space and are often incorporated in multi-shot DWEPI sequences [11, 16, 17]. The two-dimensional navigator information provides more accurate estimates of the shot-to-shot phase variation and k-space shifts in both frequency and phase encoding directions, and therefore can correct for motion in both directions. 2D navigators also enable the use of multiple diffusion gradient directions as desired.

Some implementations [12, 16, 17] use the navigator data to correct for motion in the k-space domain. The displacement of a particular shot's navigator data from the center of k-space will be equal to the displacement of the shot's image data from its true trajectory. The navigator displacement can be determined, and therefore can subsequently be used to shift the image data to its true trajectory. When shifting trajectories in the k-space domain it is necessary to perform interpolation/re-gridding of the data, since often motion will shift the k-space trajectories off the Cartesian grid. The major drawback of this approach is that interpolation and/or re-gridding techniques often lead to undesired roll-off of image intensity and additional aliasing effects [17, 20]. Additionally, the precision of estimating trajectory shifts in k-space is dependent on the resolution of k-space data, and therefore may not always be accurate [14, 17].

Other implementations use navigator information to perform direct phase subtraction (DPS) [12, 13, 23], in which the phase information from the low-resolution navigator images is directly subtracted from the high-resolution aliased images of each shot. An advantage of DPS is its capability of correcting nonlinear phase errors that can arise from non-rigid body motion (e.g. brain pulsations), which are not addressed in the other methods. Its limitation however is that the low-resolution navigator information may not correct for errors in high frequency components of the image data [13]. Additionally, the inherent undersampling of k-space data in each shot can lead to aliasing of image phase errors, in which case direct phase subtraction is no longer effective [14, 24].

More recent techniques shown to correct motion-induced phase errors use a conjugate gradient (CG) algorithm in which the navigated phase information is treated as an image encoding function in combination with the Fourier transform [19, 24]. This approach has been shown to produce superior results in comparison to the aforementioned techniques. Other implementations combine image-space phase error estimation followed by k-space correction, as in [14], and have also demonstrated success.

However, all navigator techniques still suffer from an increase in total scan time. While this can be alleviated by using self-navigated sequences in which the acquired image data is oversampled in the center of k-space providing inherent navigator information [13, 18, 19, 23], the oversampling still results in an increase in scan time and therefore decrease in scan efficiency. In order to avoid this limitation of navigators, purely iterative techniques have been proposed to correct for motion artifacts.

2.2.2 Iterative Estimation

A retrospective motion correction technique in multi-shot DWEPI without the use of navigators was first introduced by Robson et al. [22]. Their implementation characterized the acquired signal for a particular shot j affected by motion as:

$$S_j = S_o(k_x + \alpha_j, k_y + \beta_j)e^{i\phi_j} \tag{2.4}$$

where S_o is the ideal signal, the parameters α_j and β_j represent the k-space shifts due to rotation, and the parameter ϕ_j represents the global offset due to translation.

Instead of acquiring navigator data to estimate the values of these parameters, the group implemented a search technique to find the combination of values which would result in minimal image artifact. Images were reconstructed for all combinations of parameter values using a matrix inversion identical to [17]. Of all the reconstructed images, the image with minimal artifact was defined as that which has the least signal intensity in the background. The results of the study demonstrated that motion artifacts can be corrected by estimating the motion error parameters using a search procedure instead of navigators. While the procedure involves additional computational complexity, the advantage of this technique is that it does not increase scan time as navigators do.

2.3 Purpose of Study

The need for more effective methods of correcting motion artifacts in multi-shot DWI continues to grow as the clinical applications and demand of diffusion imaging increases. This study utilizes the idea of Robson et al. to develop a new and more robust iterative algorithm for correcting motion artifacts in multi-shot DWEPI, without the use of navigators and their inherent drawbacks.

The proposed method, iterative phase-cycling, offers several advantages over the aforementioned work [22]. The algorithm is completely automated, requiring no

user input to determine background regions used for calculating artifact intensity. The model implemented in this study reduces the number of searched parameters to only two (phase offset and slope) in the case of rigid body motion. Optimization techniques are included to improve efficiency and reduce computation times. Additionally, the algorithm has the capability to correct nonlinear phase errors arising from non-rigid body motion.

The following chapter describes the phase-cycling algorithm and the experimental procedures used to assess the performance of the algorithm.

3

Method

3.1 Reconstruction

Consider the case of two-shot DWEPI, in which ideal data and its artifact-free image are shown in Fig. 3.1a. Corrupted data resulting from motion and its corresponding aliased image are also shown in Fig. 3.1a. In practice we have only the corrupted data and image, and we wish to estimate the ideal unaliased image. The mathematical framework for reconstructing an artifact-free image from an aliased image is as follows, and is similar to the reconstruction method in [25] used for correcting Nyquist artifacts.

The corrupted k-space data from each shot can be split into two subsets of data: one containing positive readout lines and the other containing negative readout lines. The result is four subsets (or in general $2N$ subsets where N = number of shots) of partial k-space data. These are represented in Fig. 3.1b as S_1+, S_2+, S_1-, and S_2-, where subscripts indicate the shot number and signs indicate readout line directions. Each subset can be used to reconstruct an image (after zero-filling the data), resulting in four images with Nyquist ghosts due to the undersampling of each subset. Note that the effects of motion are not present in these images because the data in each

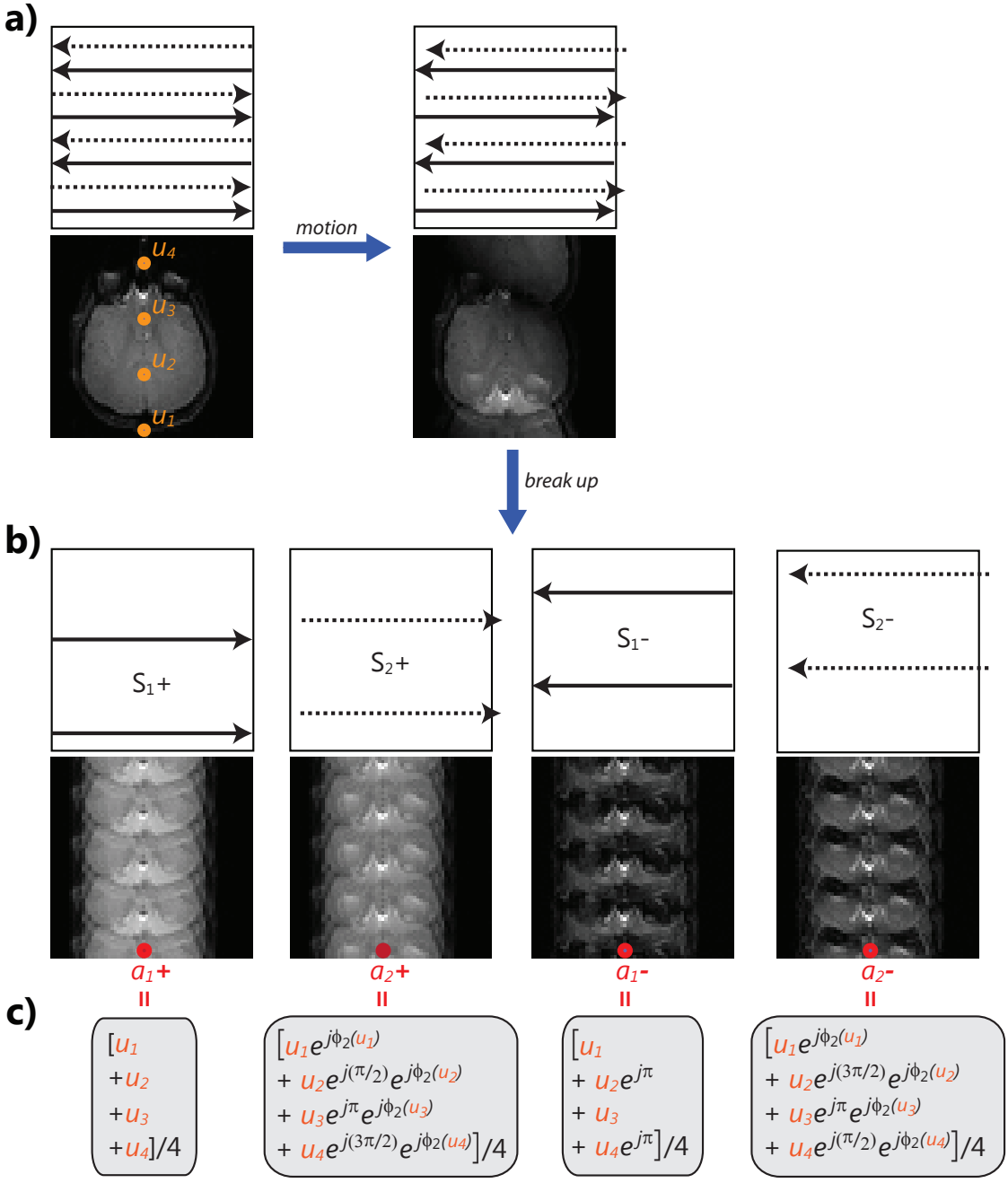

FIGURE 3.1: **(a)** Ideal two-shot EPI data and the artifact-free image (left) and corrupted two-shot data with an aliased image due to motion (right) **(b)** Corrupted data broken up into four subsets: positive and negative readout lines for each shot. The images from each subset contain overlapping Nyquist ghosts **(c)** Aliased voxel intensities in the subset images can be related to the unaliased voxels $u_1 - u_4$ in the original artifact-free image. The unaliased voxels can be calculated with the equations if the motion-induced phase error $\phi_2(\vec{u})$ is known.

subset is from a single shot. Only Nyquist ghosts are present, and therefore by Fourier transform properties it is possible to relate the signal intensities in each image to the ideal unaliased image.

Due to the overlapping Nyquist ghosts, each voxel in the four images is actually the complex summation of four different voxels separated by a quarter of FOV in the unaliased image (in N-shot DWEPI, each voxel in the $2N$ images is the complex summation of $2N$ different voxels separated by $\frac{FOV_y}{2N}$). As an example, Fig. 3.1b considers the bottom-most voxel of each ghosted image. The signal intensities of these aliased voxels a_1+, a_2+, a_1-, and a_2- are given by the sum of four voxels $u_1 - u_4$ in the unaliased image indicated by the orange dots in Fig. 3.1a, which start from the same bottom-most location and are separated by $\frac{FOV_y}{4}$. The exact equations for each aliased voxel are given in Fig. 3.1c. a_1+, the voxel from S_1+ data, is a simple magnitude summation. a_1-, the voxel from S_1- data, is a summation with phase modulation terms, which arise from the shift in k-space trajectories between S_1- and S_1+ and are given by Fourier transform properties.

The equations for a_2+ and a_2-, corresponding to S_2+ and S_2- respectively, also contain the known Fourier phase modulations due to the different trajectories of each subset. However since motion causes the second shot to be affected differently than the first the equations also contain additional motion-induced phase errors which are a function of location: $\phi_2(\vec{u})$. If these motion induced phase errors are known, either through the use of navigators or by the method presented in the next section, then the four equations can be solved for the unknown artifact-free image voxels $u_1 - u_4$. This can be represented in matrix form as:

$$\begin{bmatrix} a_1+ \\ a_2+ \\ a_1- \\ a_2- \end{bmatrix} = \frac{1}{4} \begin{bmatrix} 1 & 1 & 1 & 1 \\ e^{j\phi_2(u_1)} & e^{j\frac{\pi}{2}+\phi_2(u_2)} & e^{j\pi+\phi_2(u_3)} & e^{j\frac{3\pi}{2}+\phi_2(u_4)} \\ 1 & e^{j\pi} & 1 & e^{j\pi} \\ e^{j\phi_2(u_1)} & e^{j\frac{3\pi}{2}+\phi_2(u_2)} & e^{j\pi+\phi_2(u_3)} & e^{j\frac{\pi}{2}+\phi_2(u_4)} \end{bmatrix} \begin{bmatrix} u_1 \\ u_2 \\ u_3 \\ u_4 \end{bmatrix} \tag{3.1}$$

To reconstruct the entire artifact-free image, (3.1) must be solved for multiple locations of the aliased voxels $a_1 - a_4$ until all unaliased voxels are solved for. Because four unaliased voxels can be calculated from each aliased voxel location, it is sufficient to solve (3.1) $\frac{x_{size} \times y_{size}}{4}$ times, where $x_{size} \times y_{size}$ is the image matrix size. In the general case of N-shot DWEPI, the artifact-free image can be calculated by solving the general matrix which must be solved $\frac{x_{size} \times y_{size}}{2N}$ times:

$$\begin{bmatrix} a_1+ \\ a_2+ \\ \vdots \\ a_N+ \\ a_1- \\ a_2- \\ \vdots \\ a_N- \end{bmatrix} = \frac{1}{2N} \begin{bmatrix} e^{j\frac{0\cdot 0\pi}{N}} & e^{j\frac{0\cdot 1\pi}{N}} & \cdots & e^{j\frac{0\cdot(2N-1)\pi}{N}} \\ e^{j\frac{1\cdot 0\pi}{N}+\phi_2(u_1)} & e^{j\frac{1\cdot 1\pi}{N}+\phi_2(u_2)} & \cdots & e^{j\frac{1\cdot(2N-1)\pi}{N}+\phi_2(u_{2N})} \\ \vdots & \vdots & \ddots & \vdots \\ e^{j\frac{(N-1)\cdot 0pi}{N}+\phi_N(u_1)} & e^{j\frac{(N-1)\cdot 1\pi}{N}+\phi_N(u_2)} & \cdots & e^{j\frac{(N-1)\cdot(2N-1)\pi}{N}+\phi_N(u_N)} \\ e^{j\frac{N\cdot 0\pi}{N}} & e^{j\frac{N\cdot 1\pi}{N}} & \cdots & e^{j\frac{N\cdot(2N-1)\pi}{N}} \\ e^{j\frac{(N+1)\cdot 0\pi}{N}\phi_2(u_1)} & e^{j\frac{(N+1)\cdot 1\pi}{N}+\phi_2(u_2)} & \cdots & e^{j\frac{(N+1)\cdot(2N-1)\pi}{N}+\phi_2(u_{2N})} \\ \vdots & \vdots & \ddots & \vdots \\ e^{j\frac{(2N-1)\cdot 0\pi}{N}+\phi_N(u_1)} & e^{j\frac{(2N-1)\cdot 1\pi}{N}+\phi_N(u_2)} & \cdots & e^{j\frac{(2N-1)\cdot(2N-1)\pi}{N}+\phi_N(u_{2N})} \end{bmatrix} \begin{bmatrix} u_1 \\ u_2 \\ \vdots \\ u_{N-1} \\ u_N \\ u_{N+1} \\ \vdots \\ u_{2N} \end{bmatrix} \tag{3.2}$$

where ϕ_N is the motion-induced phase error profile for the N^{th} shot.

3.2 Iterative Phase-Cycling

In order to solve (3.2) the phase errors for all N shots must be estimated. This study proposes an iterative phase-cycling method for estimating these errors. The technique has been shown to successfully estimate phase errors arising from eddy currents and other hardware imperfections [25], but has not yet been utilized to correct motion-induced phase errors.

If the image reconstruction method described above is performed column-by-column, the phase error for the N^{th} shot can be estimated as a 1D function. For a given column in the image at a location x_0 along the frequency encoding direction, the phase error is given by:

$$\phi_N(x_o, y) = \phi_0 + g_x(x_0) + g_{x^2}(x_0)^2 + g_y y = \theta + g_y y \tag{3.3}$$

where ϕ_0 is the global phase offset arising from translation, g_x, g_y are the linear phase ramps in the frequency and phase encoding directions, respectively, arising from rotational motion, and g_{x^2} represents the nonlinear phase term in the frequency encoding direction which can arise from pulsatile motion. Since for a given column $x = x_0$ is constant, all phase terms for the frequency encoding direction are also constant and can therefore be summed with the global phase offset, resulting in a single constant θ. The result is a phase error equation consisting of only two unknown parameters, θ and g_y. Note that nonlinear phase terms in the phase encoding direction can also be accounted for, if desired, by including an additional term to the equation:

$$\phi_N(x_o, y) = \theta + g_y y + g_{y^2} y^2 \tag{3.4}$$

Accordingly this method has the potential to solve for nonlinear phase errors in both frequency and phase encoding directions.

In this study only linear phase errors in the phase encoding direction were considered as in (3.3) in order to reduce the computation cost. Each shot will have different values of the two parameters θ, g_y, and these parameters must be estimated for all shots except the first "reference" shot. Therefore in general N-shot DWEPI it is necessary to estimate $2(N-1)$ parameters for each column.

The method for estimating θ and g_y using iterative phase-cycling is as follows. In each column we cycle through a range of values $-\xi_\theta \leq \theta \leq \xi_\theta$ and $-\xi_{g_y} \leq g_y \leq \xi_{g_y}$ for both parameters and reconstruct a 1D image profile using (3.2) for all combinations of values. The ranges are cycled in discrete step sizes $\delta_\theta, \delta_{g_y}$, resulting in m and n attempted values for θ and g_y, respectively:

$$m = \frac{2\xi_\theta}{\delta_\theta} \tag{3.5a}$$

$$n = \frac{2\xi_y}{\delta_y} \tag{3.5b}$$

Therefore $(m \times n)^{2(N-1)}$ 1D image profiles are reconstructed for a column. Of these, the image profile with the least amount of residual motion artifact is defined as the one which has the least amount of background energy. Here the background energy is calculated as the summation of signal intensities from pixels in the background. Therefore the profile with minimal signal intensity from background pixels is the profile considered to have the least amount of artifact. In this study the background pixels are specified through use of a mask, which can be created by thresholding the B_0 image typically acquired in scans.

Once the profile with the least amount of artifact is determined, the corresponding values of θ and g_y which were used to reconstruct the profile are saved: this gives the phase error $\phi_N(x_0, y)$ for the particular column. The entire process is then repeated in adjacent columns until an entire image with minimal aliasing has been reconstructed and the full phase error maps have been determined.

3.3 Optimization

In order to improve computational efficiency of the iterative phase-cycling process, which can be time consuming if $(m \times n)^{2(N-1)}$ phase parameter combinations are attempted for each column, three optimization techniques can be used: range reduction for subsequent columns, sparse search, and low-resolution estimation.

3.3.1 Range Reduction

After θ and g_y values are found for the first column, the search ranges ξ_θ, ξ_{g_y} for each subsequent column can be safely reduced under the assumption that motion-induced phase errors vary slowly in the frequency encoding direction, which is typically the case. So given θ and g_y from the first column, the search in the second column is centered around those values, and the range is decreased by a factor f_{range}. Therefore the total number of combinations of θ, g_y is reduced to $\frac{(m \times n)}{(f_{range})^2}^{2(N-1)}$. All remaining

columns use the reduced search range, and for each column the range is centered around the estimated parameter values from the previous column.

3.3.2 Sparse Search

In a sparse search, the ranges of searched values ξ_θ, ξ_{g_y} are kept the same, but the step sizes $\delta_\theta, \delta_{g_y}$ are increased. Therefore the total number of searched values m, n are decreased (3.5). The parameters found to give the lowest artifact will therefore only be rough estimates, and the profile will likely have a significant level of residual artifact. However after these rough estimates are found, a fine search is performed on the same column using decreased step sizes and ranges centered around these estimates. This fine search is repeated iteratively for the column until the combination of parameter values yielding the lowest artifact no longer changes, corresponding to the minimum background energy. This method can be used in conjunction with range reduction, further optimizing the entire process, or can be used alone in each column. When used with range reduction, sparse search is only applied in the first column; all subsequent columns use a fine search with reduced range centered around the estimates of the previous column.

3.3.3 Low-Resolution Estimation

In low-resolution estimation, only a central portion of the k-space data is used in (3.2) to reconstruct low-resolution 1D image signals and estimate the phase parameters. The amount by which the original k-space data is reduced is given by a reduction factor f_{res}. Phase-cycling is performed on the low-resolution aliased image to create a low-resolution phase map; this low-resolution phase map is then extended to full resolution using fitting, and the high-resolution unaliased image is reconstructed using the fitted map and the original full k-space data. This technique can be used in conjunction with range reduction and/or sparse search.

3.4 Phase Fitting

After estimates of θ, g_y for all columns have been determined using phase-cycling the final phase map appears very discrete, due to the discrete step sizes used in phase-cycling. Polynomial fitting can be used to smoothen the discrete phase map into a more continuous map. In this study fitted phase maps were used to reconstruct all images, however the difference between using the initial maps and fitted maps is negligible when the phase-cycling step sizes are adequately small. Fitting is also necessary when low-resolution estimation is used, as described above.

3.5 Experimental Method: Two-Shot Correction

The capabilities of iterative phase-cycling and the optimization procedures were tested first for the case of two-shot DWEPI, using simulated data and hybrid-simulated data. All processing and correction was performed using MATLAB (Mathworks, Natick, MA).

3.5.1 Simulated Motion Artifact

To initially test the feasibility of the reconstruction method and iterative phase-cycling, mathematically created motion-induced phase errors were added to artifact-free, non diffusion-weighted EPI data (matrix size = 64 X 64, FOV = 24 cm, slice thickness = 4 mm, TR = 2 sec, TE = 26 ms).

Simulated motion-artifacts were induced by first separating the EPI data into subsets of alternating lines, as in interleaved two-shot EPI. From one of these subsets an image was reconstructed and phase gradients applied to the image. The phase modified image was then Fourier-transformed back to k-space, combined with the unaltered subset, and the full data was then reconstructed to produce an image with simulated motion artifacts arising from the introduced phase differences between

"shots". Five cases of phase errors were applied:

1. Linear error in frequency encoding direction: $g_x = \frac{\pi}{x_{dim}} = \frac{\pi}{64}$
2. Linear error in phase encoding direction: $g_y = \frac{\pi}{y_{dim}} = \frac{\pi}{64}$
3. Linear errors in frequency and phase encoding directions: $g_x = g_y = \frac{\pi}{64}$
4. Nonlinear error in frequency encoding direction, linear error in phase encoding direction: $g_{x^2} = \frac{\pi}{64}, g_y = \frac{\pi}{64}$
5. Nonlinear errors in frequency and phase encoding directions: $g_{x^2} = \frac{\pi}{64}, g_{y^2} = \frac{\pi}{64}$

These values of phase errors were chosen to simulate typical values in actual multi-shot conditions, and were compared with values found from the hybrid-simulations for verification.

Iterative phase-cycling was performed using (3.3). Note that (3.3) only considers linear phase errors along the phase encoding direction, and therefore Case 5 above is meant to assess the error of using the linear model when nonlinear terms are present.

Only range reduction was applied as an optimization procedure, with $f_{range} = 4$. The phase-cycling parameters used were: $(\xi_\theta = \pi, \xi_{g_y} = \frac{\pi}{64}, \delta_\theta = \frac{2\pi}{60}, \delta_{g_y} = \frac{2\pi}{64\times 60})$. Therefore, from (3.5), 3600 phase combinations/1D profiles are searched in the first column, and $\frac{3600}{{f_{range}}^2} = 225$ are searched in all subsequent columns. For comparison, phase-cycling was also performed without range reduction (i.e. 3600 searches in every column), and differences in computation time and residual error were calculated between the two methods.

The ability of phase-cycling to remove artifacts for all cases was assessed using the normalized root mean squares error (NRMSE) between the reconstructed and original image, and was calculated as:

$$NRMSE = \frac{||I_r - I_0||_F}{||I_0||_F} \tag{3.6}$$

where I_r is the reconstructed image after phase-cycling, I_0 is the original artifact-free image before motion simulation, and $||\cdot||_F$ is the Frobenius norm of a matrix, which is defined as the square root of the sum of the squares of its elements, i.e.

$$||A||_F = \sqrt{\sum_{i=1}^{x_{dim}} \sum_{j=1}^{y_{dim}} |a_{i,j}|^2} \tag{3.7}$$

The NRMSE was also used to assess the difference between the applied phase maps to introduce motion artifacts and the estimated phase maps after phase-cycling.

3.5.2 Hybrid-Simulations

Following testing of phase-cycling with the pure simulations above, hybrid-simulations were performed to assess the performance of the technique with realistic aliased data. Single-shot DWEPI images were acquired (GE 3 Tesla) (Matrix size = 128 x 128, FOV = 24 cm, slice thickness = 4 mm, TR = 5 sec, TE = 90 ms, b-factor = 1000 s/mm^2) with an eight-channel coil at eight time points ($t_1 - t_8$).

The single-shot data at all time points were free of artifact. However, slight motion between the time points results in phase differences among the images, just as motion between shots in multi-shot DWEPI result in phase differences. Two-shot hybrid-simulation consists of combining alternating lines of k-space data from two different time points, resulting in a reconstructed image containing artifacts due to the motion-induced differences between the time points. The advantages to performing hybrid-simulations are that it produces realistic data similar to true multi-shot DWEPI, and it provides a gold standard (the unaliased single-shot image) to compare the correction results with.

Hybrid-simulation of eight aliased images were created using eight combinations of the time points: $(t_1, t_2), (t_3, t_4), (t_5, t_6), (t_7, t_8), (t_1, t_8), (t_2, t_7), (t_3, t_8)$, and (t_4, t_7).

Optimization Testing

Prior to correcting artifacts from all eight combinations, optimization techniques were first tested and compared on one of the eight aliased images. The techniques were grouped into three procedures: range reduction with low-resolution estimation, sparse search with low-resolution estimation, and sparse search with both range reduction and low-resolution estimation.

Phase-cycling parameters for the three optimization procedures were as follows. Parameters in range reduction with low-resolution estimation were: ($f_{range} = 4, \xi_\theta = \pi, \xi_{g_y} = \frac{\pi}{y_{dim}}, \delta_\theta = \frac{2\pi}{60}, \delta_{g_y} = \frac{2\pi}{y_{dim} \times 60}$), where y_{dim} is given by the spatial resolution used in low-resolution estimation.

Initial parameters in sparse search with low-resolution estimation were: ($\xi_\theta = \pi, \xi_{g_y} = \frac{\pi}{y_{dim}}, \delta_\theta = \frac{2\pi}{6}, \delta_{g_y} = \frac{2\pi}{y_{dim} \times 6}$). Step sizes used in the fine search after the initial sparse search were ($\delta_\theta = \frac{2\pi}{60}, \delta_{g_y} = \frac{2\pi}{y_{dim} \times 60}$).

Parameters in sparse search with range reduction and low-resolution estimation were the same as sparse search alone, but with $f_{range} = 2$.

Low-resolution estimation was applied at five levels: $f_{res} = 1$ (i.e. no reduction), 2, 4, 8, and 16, yielding spatial resolutions of 128x128, 64x64, 32x32, 16x16, and 8x8, respectively. Comparisons of computation time and residual error were made for each of the three optimization procedures at each resolution level.

Additional Methodology

After comparison of optimization procedures, all the remaining seven images were corrected using phase-cycling with sparse search and range reduction without low-resolution estimation (i.e. $f_{res} = 1$). All initial parameter values were equivalent to those listed above. NRMSEs were calculated between the hybrid-simulated aliased images and the gold standard single-shot image, and between the corrected images

and the gold standard. Corrected images which still had significant residual error ($NMRSE \geq 0.3$) were corrected again using a larger search range for g_y ($\xi_{g_y} = \frac{4\pi}{128}$).

Phase-cycling correction was performed only on data from a single coil channel of each image. The estimated phase maps were then applied to correct data from all coil channels, and the images from each channel were subsequently combined (using sum-of-squares) to form the final corrected image.

3.6 Experimental Method: Four-Shot Correction

The ability of phase-cycling to correct motion artifacts in four-shot DWEPI was tested using simulated data, hybrid-simulated data, and true four-shot DWEPI data. The increase in computational complexity to estimate phase parameters in four-shot DWEPI compared to two-shot DWEPI is addressed in the methodology. All processing and correction was performed using MATLAB.

3.6.1 Computational Complexity

In the two-shot cases it was not particularly necessary to apply optimization techniques, aside for convenience only. This differs from the four-shot case, in which it becomes very necessary to use optimization techniques.

For the case of two-shot correction, only two phase parameters need to be searched for: θ and g_y for the second shot, resulting in a two-dimensional search problem. For the case of four-shot data, θ and g_y must be found for the second, third, and fourth shots, resulting in a six-dimensional search problem. Without any optimization techniques, this would require a search of $(m \times n)^6$ phase combinations/1D image profiles for each column, as described in Section 3.2. If m and n are large as in the unoptimized two-shot case ($m = n = 60$), the computation time needed to attempt all combinations would be significant and the phase-cycling technique would no longer be practical.

To address this, all four-shot corrections (simulated, hybrid-simulated, and true data) were done using some combination of the three optimization techniques in conjunction. Differences in residual error/computation time between optimization combinations were addressed for each experiment.

3.6.2 Simulated Motion Artifact

Motion artifacts were mathematically introduced to the same artifact-free EPI data as in Section 3.5.1. The general method of simulation is the same, this time separating the EPI data into four subsets of alternating lines and applying different phase ramps to the subset images before recombining the data. Because the ability of phase-cycling to correct for linear/nonlinear phase errors is the same for any number of shots, it was not deemed necessary to test for multiple cases of phase errors as was done in the two-shot correction. Only one case was considered for the simulated four-shot data: linear phase errors in both frequency and phase encode directions. The phase errors applied to three of the four "shots" were:

- Second Shot: $g_x = g_y = \frac{0.6\pi}{64}$
- Third Shot: $g_x = g_y = \frac{0.8\pi}{64}$
- Fourth Shot: $g_x = g_y = \frac{\pi}{64}$

Correction was done using sparse search with range reduction and low-resolution estimation. Phase-cycling parameters used in sparse search were: $(\xi_\theta = \pi, \xi_{g_y} = \frac{\pi}{y_{dim}}, \delta_\theta = \frac{2\pi}{6}, \delta_{g_y} = \frac{2\pi}{y_{dim}\times 6})$, where y_{dim} is given by the spatial resolution used in low-resolution estimation. Step sizes used in the fine search after the initial sparse search were $(\delta_\theta = \frac{2\pi}{60}, \delta_{g_y} = \frac{2\pi}{y_{dim}\times 60})$.

Range reduction was done with $f_{range} = 1.2$. Low-resolution estimation was performed using reduction factors of $f_{res} = 2$ and 4, yielding spatial resolutions of 32x32 and 16x16 respectively.

3.6.3 Hybrid-Simulations

Hybrid-simulations were performed using the same data as in the two-shot case. Data from four time points are combined to simulate aliased four-shot DWEPI images. Three combinations of time points were used: $(t_1, t_2, t_4, t_6), (t_1, t_2, t_7, t_8)$, and (t_2, t_4, t_6, t_8).

Optimization techniques were first tested and compared with one of the three images. The techniques were grouped into two procedures: sparse search with range reduction and low-resolution estimation, and sparse search alone for comparison.

Initial parameters in the sparse searches were: $(\xi_\theta = \pi, \xi_{g_y} = \frac{\pi}{y_{dim}}, \delta_\theta = \frac{2\pi}{6}, \delta_{g_y} = \frac{2\pi}{y_{dim} \times 6})$. Step sizes used in the fine search after the initial sparse search were $(\delta_\theta = \frac{2\pi}{60}, \delta_{g_y} = \frac{2\pi}{y_{dim} \times 60})$.

Range reduction was done with $f_{range} = 2$. Low-resolution estimation was performed using reduction factors of $f_{res} = 1$, 2, and 4, yielding spatial resolutions of 128x128, 64x64, and 32x32, respectively.

Additional Methodology

After optimization comparisons, the remaining two images were corrected using phase-cycling with sparse search combined with range reduction and low-resolution estimation ($f_{range} = 2, f_{res} = 2$). Phase-cycling correction was performed only on data from a single coil channel, and the resulting phase maps were used to correct data from all coil channels before reconstructing the final corrected image.

3.6.4 True Four-Shot DWEPI data

Following experiments with hybrid-simulated data, actual four-shot DWEPI data (matrix size = 256x256) containing motion artifacts were corrected using phase-cycling. Sparse search and range reduction were used with low-resolution estimation ($f_{res} = 4$), and also without low-resolution estimation for comparison. Search pa-

rameters were: $(\xi_\theta = \pi, \xi_{g_y} = \frac{4\pi}{256}, \delta_\theta = \frac{2\pi}{6}, \delta_{g_y} = \frac{8\pi}{256\times 6})$. Step sizes used in the fine search after the initial sparse search were: $(\delta_\theta = \frac{2\pi}{60}, \delta_{g_y} = \frac{2\pi}{256\times 60})$.

Because no gold standard image is available for this experiment, the criterion used for assessing the artifact levels of the aliased and corrected images was ghost-to-noise ratio (GNR):

$$GNR = 0.65 \times \frac{\mu_{ghost}}{\sigma_{noise}} \tag{3.8}$$

where μ_{ghost} is the average signal intensity in a manually chosen region of interest containing artifacts, and σ_{noise} is the standard deviation of signal intensity in a background region. The reduction of GNR between aliased and corrected images was calculated to evaluate the ability of phase-cycling to remove motion artifacts.

4

Results

4.1 Two-Shot Correction

4.1.1 Simulations

Fig. 4.1 is the clean non diffusion-weighted EPI image used for motion simulations. It is used as the ground truth image when calculating errors in simulated and corrected images.

The five applied phase error cases and the resulting images are shown in Fig. 4.2a. The simulated images contain high levels of artifact and high NRMSE. Fig. 4.2b shows the corrected images and estimated phase maps following phase-cycling with range-reduction.

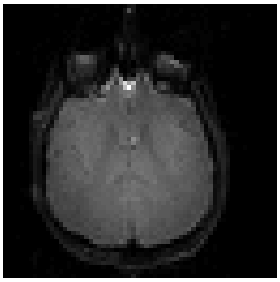

FIGURE 4.1: Original artifact-free EPI image used in simulating motion-artifacts.

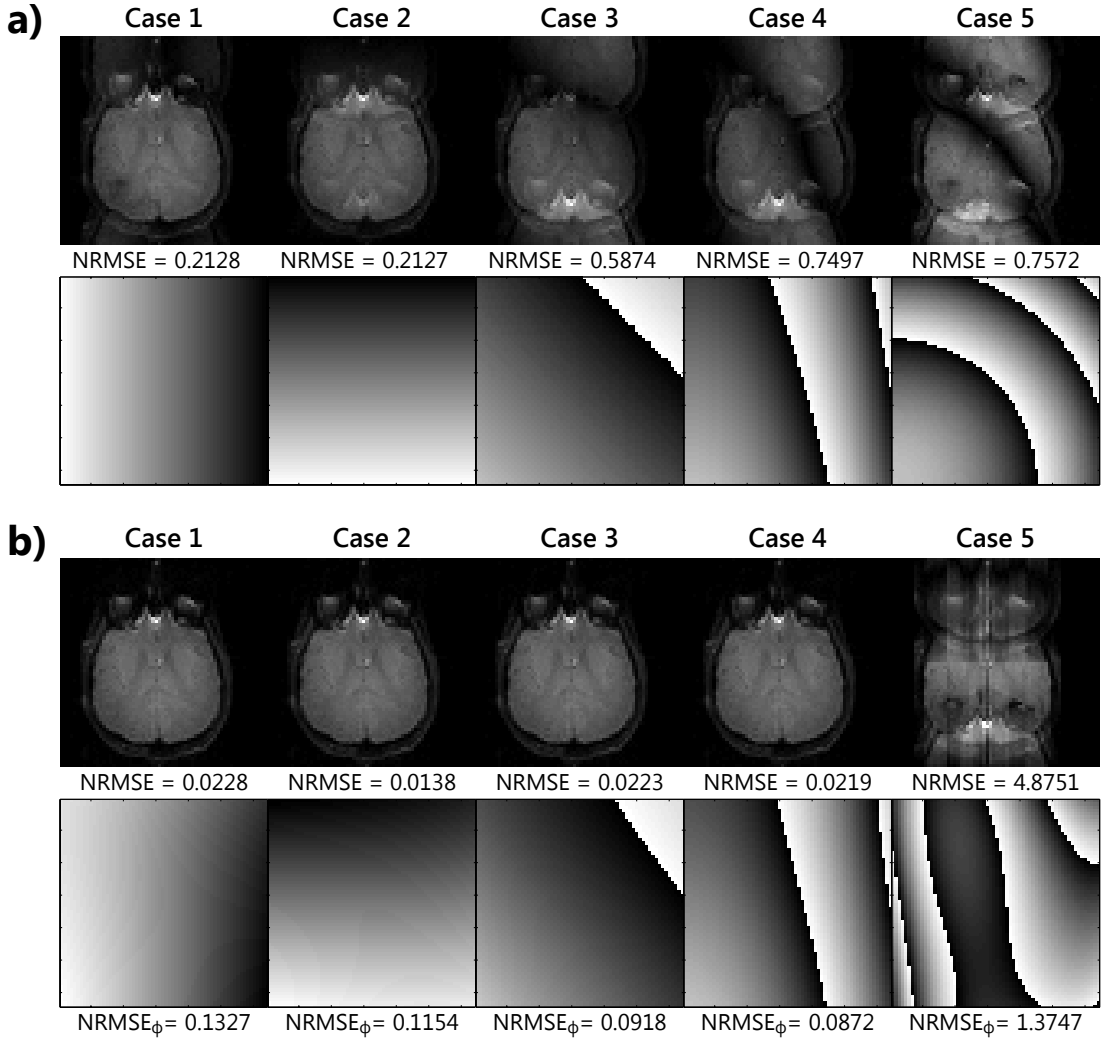

FIGURE 4.2: **(a)** Images with simulated motion-artifacts (top row) introduced by mathematically applying phase gradients (second row) to the original data in Fig. 4.1 **(b)** Corrected images and estimated phase errors after phase-cycling, showing reduced artifact in Cases 1-4. Case 5 (rightmost column) could not be corrected.

The NRMSEs after correction are significantly reduced in Cases 1-4 and the images are free of artifact. The difference among errors in these cases is negligible and the corrected images are virtually identical. The phase maps estimated by phase-cycling (bottom row) closely resemble the applied phase errors (second row) and the corresponding NRMSEs are small.

The motion artifacts from Case 5, which had nonlinear terms along y in the

applied phase error, could not be corrected using the linear model of phase-cycling, and the resulting image and estimated phase map have severe errors.

Computation times for all images were approximately $T \approx 4.2$ seconds. For comparison, corrections were also done using phase-cycling without range-reduction. The results were identical to those in Fig. 4.2b, however computation times were notably longer, at approximately $T \approx 45$ seconds.

4.1.2 Hybrid-Simulations

Fig. 4.3 shows an artifact-free single-shot DWEPI image from one time point t_1, and a hybrid-simulated image containing motion artifacts after combining data from t_1 with data from another time point t_2. Also shown is the phase difference between the images from both time points. The phase difference is linear and slowly-varying, indicating that the linear model of phase-cycling should be able to correct the aliased image.

The results of phase-cycling using the three optimization procedures at multiple levels of low-resolution estimation are shown in Fig. 4.4.

From Fig. 4.4 it is apparent that the use of low-resolution phase estimation can

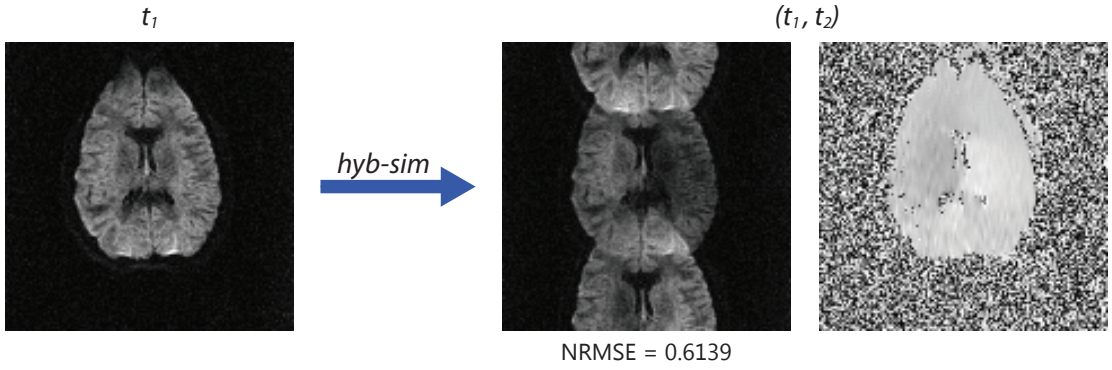

FIGURE 4.3: Hybrid-Simulation: Data from an artifact-free image at one time point (left) is combined with the data of another time point (not shown) to create an image with simulated motion artifacts (middle). The difference in phases (right) between the two time points is approximately linear.

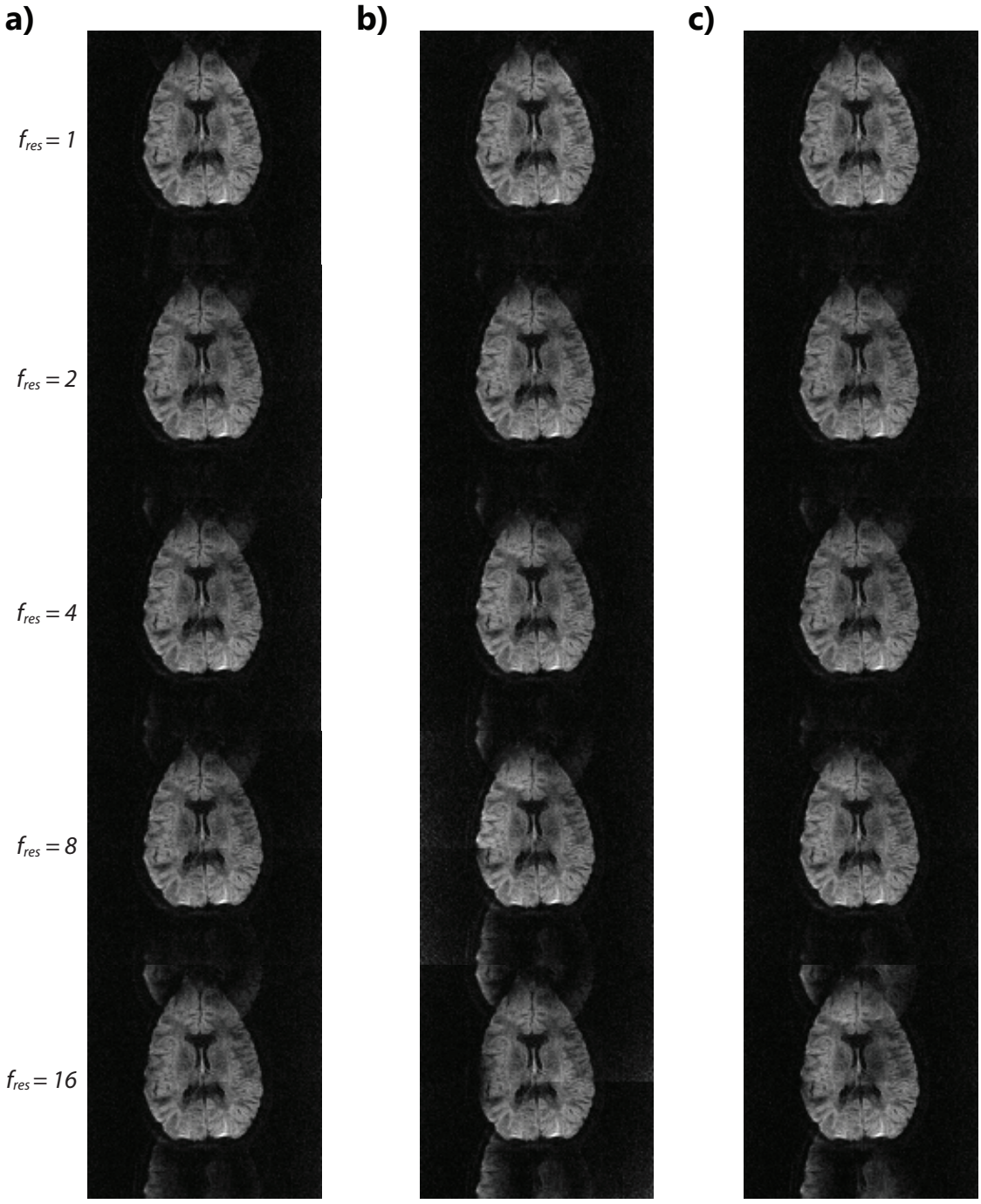

FIGURE 4.4: Correction of the aliased image from Fig. 4.3 using three optimization procedures at five levels of low-resolution estimation: **(a)** Range reduction **(b)** Sparse search **(c)** Sparse search with range reduction

result in residual artifacts for all optimization procedures. When the resolution reduction factor $f_{res} = 16$, corresponding to a matrix size of only 8x8, residual image artifacts are the most severe. The use of higher-spatial resolutions (lower f_{res}) enables more accurate estimations of the phase error, and hence less residual artifact. Fig. 4.5 depicts the process of low-resolution estimation for the case of $f_{res} = 2$.

Table 4.1 includes the errors and computation times of the reconstructed images from Fig. 4.4. Sparse search with range reduction was found to be the most advantageous of the three optimization procedures, with similar residual errors as the other two procedures, but significantly smaller computation times. It can also be seen that low-resolution estimation resulted in reduced computation times, but at the cost of increased residual errors.

To further verify the accuracy of sparse search, phase-cycling was performed without any optimization and the background energies for each combination of θ

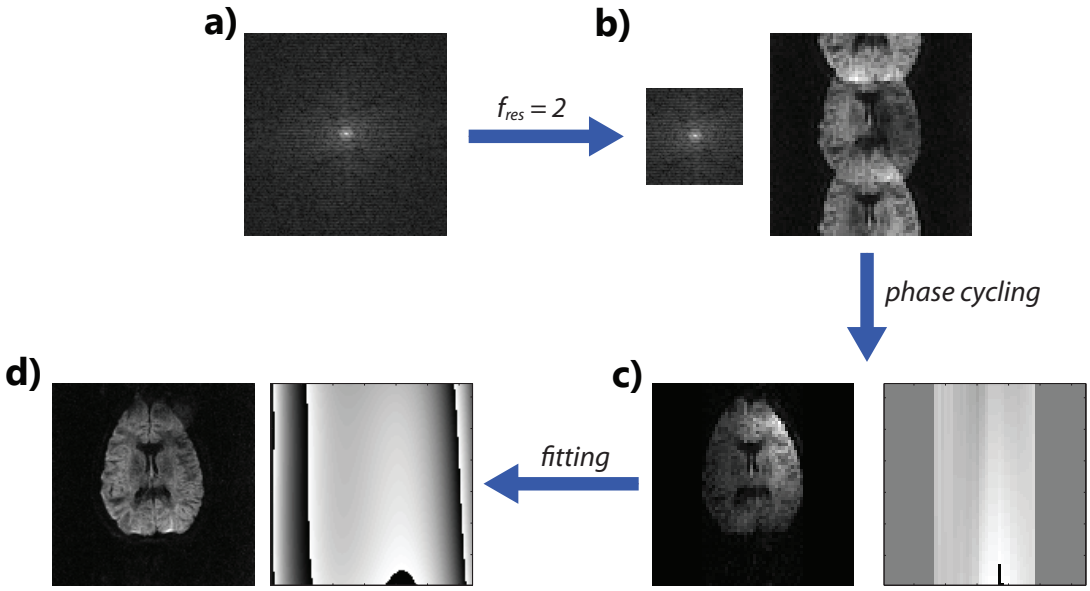

FIGURE 4.5: Low-resolution estimation process with $f_{res} = 2$: **(a)** Aliased 128x128 k-space data **(b)** Extracted central k-space data of size 64x64 and resulting low-resolution aliased image **(c)** Low-resolution phase map estimation and corrected image following phase-cycling **(d)** Full resolution phase map acquired after fitting and the corresponding full resolution image.

Table 4.1: NRMSEs and computation times of range-reduction *(RR)*, sparse search *(SS)*, and sparse search with range reduction *(SS+RR)*, for the images in Fig. 4.4

f_{res}	**NRMSE** (a.u.)			**Comp. Time** (secs)		
	RR	*SS*	*SS+RR*	*RR*	*SS*	*SS+RR*
1	0.126	0.120	0.124	12.71	3.83	1.81
2	0.167	0.166	0.167	4.03	1.57	1.13
4	0.177	0.176	0.173	1.95	1.04	0.93
8	0.173	0.239	0.174	1.37	0.93	0.89
16	0.216	0.293	0.278	1.09	0.85	0.86

and g_y were plotted for all columns. Fig. 4.6 shows the background energy plot from the center column and the (θ, g_y) found to yield the minimum energy, and hence the lowest artifact for the column. The non-existence of local minima is an important condition when using sparse search because of the large initial step sizes, which could result in the selection of an energy near a local minimum instead of the global minimum. This would lead to an incorrect estimation of phase parameters in the subsequent fine search, and the reconstructed image would contain residual artifacts. However it can be seen in Fig. 4.6 that there are no local minima, only a global minimum energy. Plots from all other columns and for several other images produced similar results. These findings indicate that sparse search can be safely used without the risk of selecting local minima.

The seven remaining hybrid-simulated images are shown in Fig. 4.7a. Also shown are the phase differences between the time points used to simulate each aliased image. Corrected images following phase-cycling with sparse search and range reduction ($f_{res} = 1$) are shown in Figs. 4.7b-c. Of the seven images, three could be corrected using the initial phase-cycling parameters: $(t_1, t_8), (t_3, t_8)$, and (t_4, t_7). From Fig. 4.7a it can be seen that the phase differences in these cases are linear and slowly-varying. Computation times for these images were all approximately 1.8 seconds.

Three other aliased images, $(t_3, t_4), (t_7, t_8)$, and (t_2, t_7), still had significant resid-

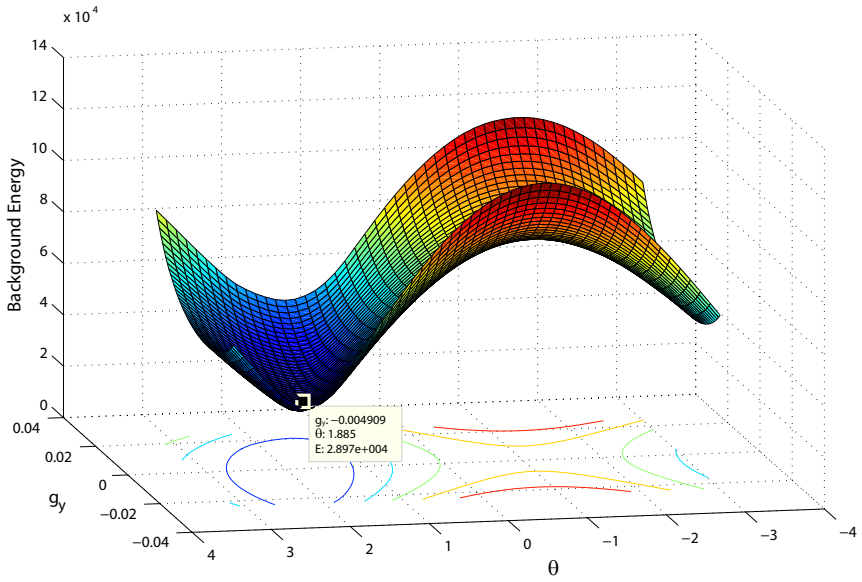

FIGURE 4.6: Plot of background energies as a function of (θ, g_y). The phase parameters found to yield the lowest background energy were $\theta = 1.885, g_y = \frac{12\pi}{128x60}$. The absence of local minima is essential for use of sparse search optimization.

ual artifact ($NRMSE \geq 0.3$) after the initial phase-cycling correction. Looking at the phase differences for these cases, it is apparent that while the errors look approximately linear, the slope g_y is much greater than in the previous three cases and phase errors vary more quickly. Phase-cycling was therefore performed again, but with a larger search range for g_y: $\xi_{g_y} = \frac{4\pi}{128}$. The results of the second correction are shown in Fig. 4.7c. The residual artifacts and calculated NRMSEs are significantly decreased using the larger search range. The increase in search range also increased computation times for these images to approximately 2.2 seconds.

One of the aliased images, (t_5, t_6), could not be corrected even with an increased search range. It can be seen from the phase difference for this case that the phase error contains nonlinearity. The linear model of phase-cycling used in this study is therefore unable to properly estimate the phase error in this particular case, and the resulting image still contains severe artifacts.

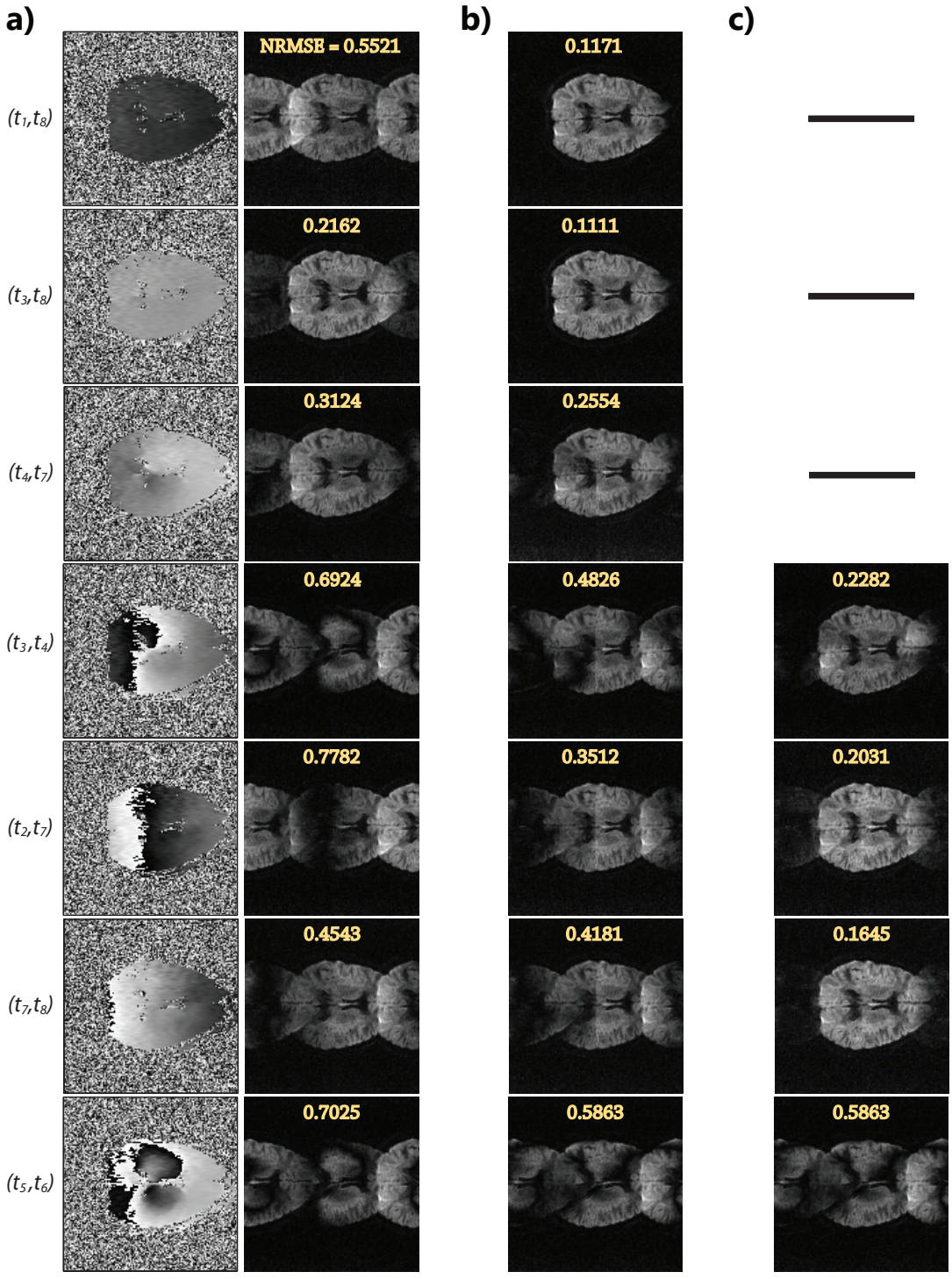

FIGURE 4.7: Correction of remaining hybrid-simulations **(a)** Phase differences and aliased images **(b)** Corrected images after phase-cycling with $\xi_{g_y} = \frac{2\pi}{128}$, in which four cases still had significant error. **(c)** Attempted correction of the four uncorrected cases in (b) using $\xi_{g_y} = \frac{2\pi}{128}$. Three show reduced artifact, while one remains uncorrected due to phase nonlinearity.

4.2 Four-Shot Correction

4.2.1 Simulations

Fig. 4.8 shows the simulated four-shot motion artifacts introduced to clean EPI data, and correction of the artifacts with phase-cycling (using sparse search and range reduction) at two levels of low-resolution estimation.

Phase-cycling correction was able to reduce the error in the aliased image significantly from $NRMSE = 1.1616$ to 0.2019 and 0.5881 (Fig. 4.8b), however the computation times were much longer than in the two-shot case, ranging on the order of minutes. It can be seen from the computation times of $f_{res} = 2$ and $f_{res} = 4$ that the time-saving ability of low-resolution estimation becomes much more significant in the four-shot case. However just as in the two-shot case, the time-savings comes at a cost of increased residual error, which in this particular experiment was notably high with a threefold increase in NRMSE from $f_{res} = 2$ to $f_{res} = 4$.

4.2.2 Hybrid-Simulations

The correction of a four-shot hybrid-simulated image with motion artifacts is shown in Fig. 4.9. Artifacts in the aliased image, produced by combining data from time points t_1, t_2, t_4, t_6, are severe and prevent adequate visibility of brain structure. Corrected images after phase-cycling (with sparse search and range reduction) are vir-

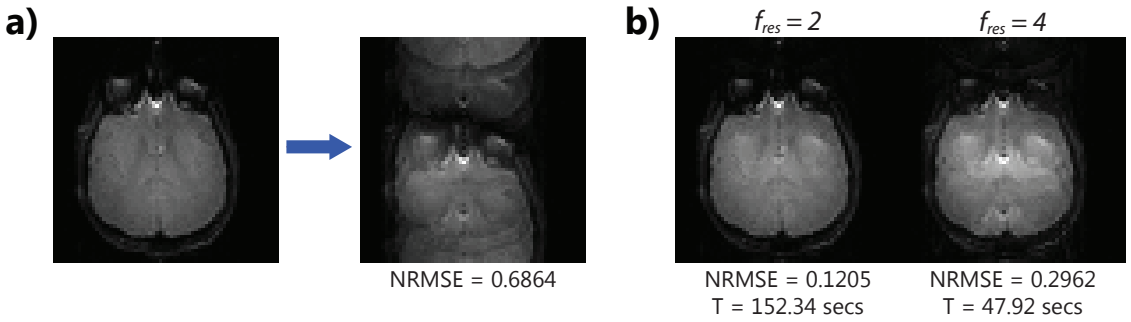

FIGURE 4.8: **(a)** Simulation of four-shot motion artifacts using clean EPI data **(b)** Corrected images after phase-cycling at two levels of low-resolution estimation.

tually free of artifacts and resemble the original single-shot DWEPI image where brain structure is clearly visible. The NRMSEs for corrected images at all levels of low-resolution estimation are low (≤ 0.3), although the image reconstructed with $f_{res} = 4$ shows an increase in background noise which can be attributed to phase-fitting errors.

The results of this hybrid-simulation again demonstrate the trade-off between computation time and residual error when using low-resolution estimation. However since the increase in error between $f_{res} = 1$ and $f_{res} = 2$ is negligible ($\Delta NRMSE \leq 0.01$) compared to the large reduction in computation time ($\Delta T \approx 1min$), all subsequent hybrid-simulations were corrected using $f_{res} = 2$.

Fig. 4.10 shows two additional hybrid-simulated images and their corrected coun-

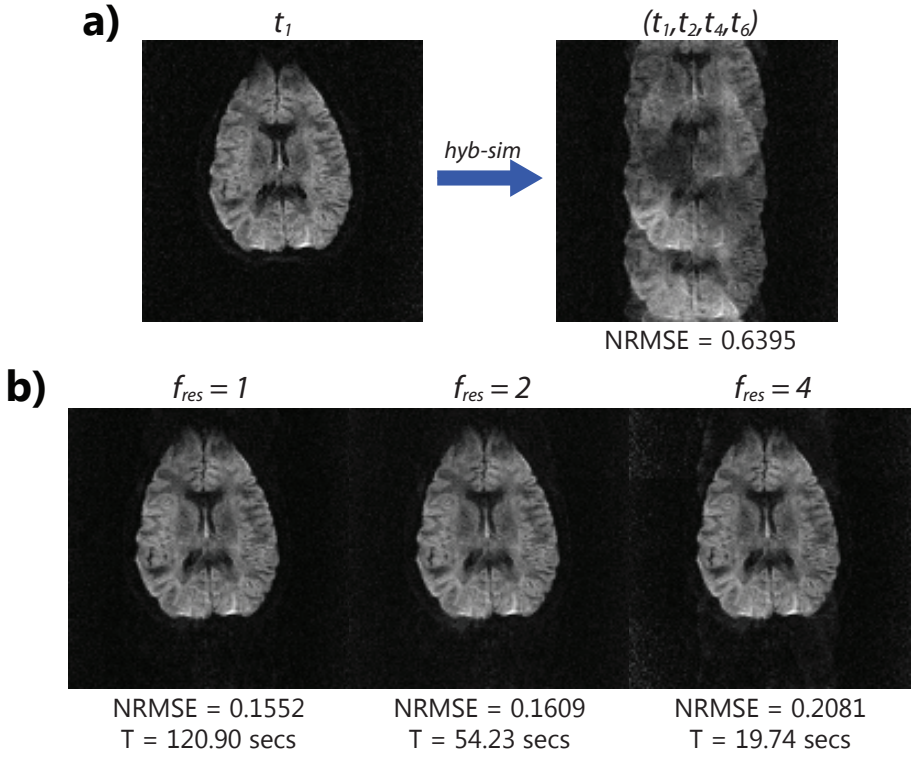

FIGURE 4.9: **(a)** Hybrid-simulation of four-shot motion artifacts by combining single-shot DWEPI data from four time points (image from only one time point shown) **(b)** Corrected images after phase-cycling at three levels of low-resolution estimation.

terparts. The severe artifacts in the simulated images are suppressed after phase-cycling, and the errors between the simulated images and original DWEPI image are reduced greatly. Phase-cycling in both cases took approximately 55 seconds.

4.2.3 True Four-Shot DWEPI Correction

Fig. 4.11 shows actual four-shot DWEPI containing motion-induced artifacts (top) and the images reconstructed after phase-cycling correction (bottom). The ghost and background regions used to calculate the GNRs of each image are shown in red and yellow, respectively, in the top left image. GNRs of the original aliased images from left to right were: 4.11, 5.86, and 5.43. GNRs of the corresponding corrected images were: 3.38, 3.56, and 3.71.

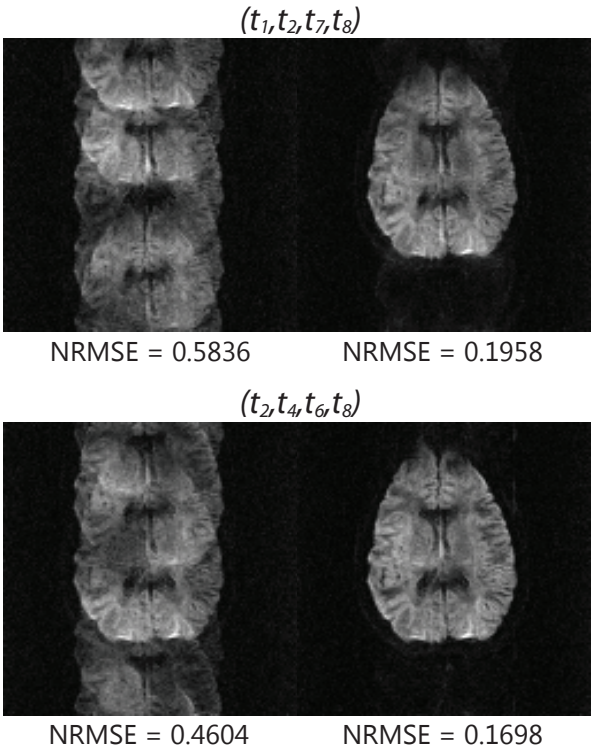

FIGURE 4.10: Additional four-shot hybrid-simulations (left column) and the corrected images (right column). Both cases show reduced image artifacts and NRMSE improvement after phase-cycling. Computation times for both images were approximately 55 seconds.

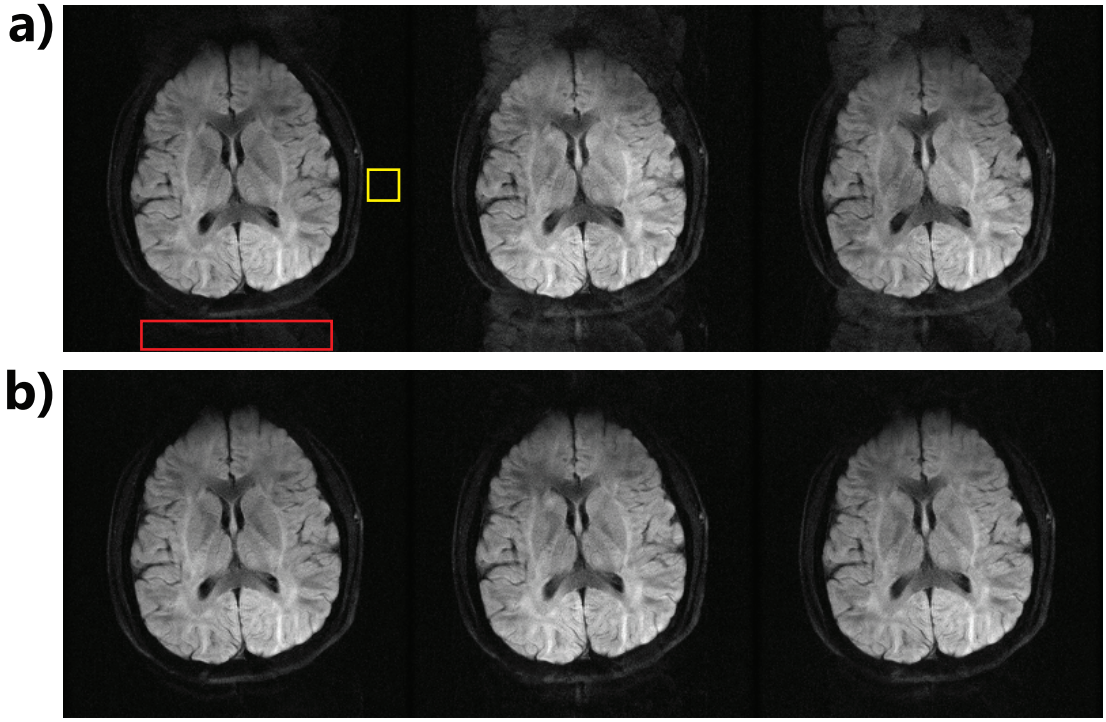

FIGURE 4.11: **(a)** True four-shot DWEPI images containing motion artifacts. **(b)** Corrected images after phase-cycling with $f_{res} = 4$. Computation time was approximately 8 minutes for each of the images

For each of the corrected images phase-cycling was performed on all eight coils individually. The computation time to correct each image was approximately 8 minutes (1 minute per coil). For comparison, correction of the center image in Fig. 4.11a was also done without low-resolution estimation. The resulting image was nearly identical to the corrected image using $f_{res} = 4$ and showed no significant improvement in suppressing artifacts (GNR = 3.5), however the computation time increased greatly to approximately 1.3 hours (10 minutes per coil).

5

Discussion

5.1 Findings

The results of experiments with simulated, hybrid-simulated, and actual multi-shot DWEPI data demonstrate the ability of phase-cycling correction to estimate motion-induced phase errors and effectively reduce artifacts.

Simulation results were able to confirm the assumption that the linear model of phase-cycling can correct for linear and nonlinear errors along the frequency encoding direction, and for linear errors along the phase encoding direction. However it was also established that the model cannot correct for nonlinear errors along the phase encoding direction (Fig. 4.2, right column), and the residual artifacts in this case are quite severe. In spite of this limitation, the linear model of phase-cycling was found to be sufficient in the majority of cases.

The optimization techniques employed with phase-cycling were found to be very advantageous, and the experiments verified the credibility of using such techniques. Hybrid-simulations illustrated that phase errors arising from motion do vary slowly along the frequency encoding direction (Fig. 4.7) as initially proposed, indicating that the range reduction technique is safe to use. The absence of local minima in

background energy plots (Fig. 4.6) confirmed the ability of sparse search to accurately find phase error parameters yielding the least artifact. This finding is especially important, as it permits the use of even larger search ranges and step sizes without the risk of selecting inaccurate values for θ or g_y. The use of large search ranges and step sizes is crucial when basic phase error information is not known a priori, which is normally the case. For these reasons much larger values of ξ_{g_y} and δ_{g_y} were used in correcting the actual four-shot DWEPI than in the hybrid-simulations. A fact of key importance with sparse search is that increasing the search range does not increase computation time as long as the step size is increased by the same factor. This is because the number of searched values remains the same, since it is simply the ratio of search range to step size as given by (3.5). As a result sparse search is extremely advantageous for estimating phase errors, particularly when considering four (or more) shot DWEPI where the number of phase parameter combinations which must be searched increases exponentially.

The only optimization technique which presented a trade-off between computational savings accuracy was low-resolution estimation. This is particularly apparent when correcting data with smaller matrix sizes (64x64 - 128x128), as in the correction of the simulations and hybrid-simulations. However for higher resolution images, as in the actual four-shot DWEPI data, the effect is less severe due to the larger matrix size (256x256) which provides enough information even at reduction factors of $f_{res} = 4$ to estimate phase errors. This finding is particularly important because it demonstrates that low-resolution estimation is still advantageous for high resolution DWI images. Additionally, it is important to note that the accuracy/efficiency compromise in phase-cycling when using low-resolution estimation is only relevant to image reconstruction and does not affect the actual scan procedure in any way. This is in contrast to the use of navigators, which have an accuracy/efficiency trade-off that does affect the scan procedure.

Compared to the originally proposed iterative method for correcting motion artifacts [22], the results of phase-cycling demonstrate several distinct advantages. First, the calculation of background energies in this method is fully automated through use of a mask, and requires no user input for selecting background regions. Second, the model used here has demonstrated the ability to correct for nonlinear errors in the frequency encoding direction, which is not possible in [22].

Furthermore, the phase-cycling technique has markedly improved computation times. In [22] the computation time to correct 256x256 four-shot DWEPI images was approximately 1 hour, even when using just the low resolution data (32x32). In contrast, the phase-cycling method was able to correct 256x256 four-shot DWEPI images in $\sim$10 minutes. The savings in computation time can be attributed to two factors, one of which is the thorough use of optimization procedures in this study. The other factor is the reduced number of error parameters which are searched. In [22] error estimation is done in k-space and three parameters must be searched: trajectory shifts in x and y and the global phase offset. The method presented here requires a search of only two parameters in image-space and is one of the advantages of column by column reconstruction in phase-cycling.

5.2 Limitations

The major limitation of this phase-cycling model is its inability to correct nonlinear phase errors along the phase encoding direction y. While the assumption of only linear errors (i.e. rigid body motion) along y was generally valid for many of the experiments in this study, in cases where non-rigid body motion is significant it will become necessary to account for nonlinear phase errors. As described in Chapter 3.2, phase-cycling has the potential to estimate nonlinear errors along y by including an additional term in the phase function for a given column:

$$\phi_N(x_o, y) = \theta + g_y y + g_{y^2} y^2 \tag{5.1}$$

The computational requirements increase significantly when considering the extra nonlinear term g_{y^2}. The number of phase combinations, and hence the number of 1D image profiles reconstructed for each column, increases when three parameters are considered. Two-shot correction becomes a three-dimensional search problem, instead of two-dimensional when using the linear model, and four-shot correction becomes a nine-dimensional search problem instead of six-dimensional. Because of this additional computational complexity, the use of optimization techniques will be increasingly important for this model, especially with higher-shot acquisitions.

5.3 Potential Developments

A benefit of the phase-cycling method is that it can easily be combined with other correction and acquisition techniques. If the requirements for processing time are stringent, phase-cycling can actually be combined with 1D navigator estimation. 1D navigators do not greatly increase scan time, and may provide enough phase information to estimate the global offset and nonlinear phase error along the frequency direction. This means θ can be estimated using a 1D navigator and only g_y must be estimated with phase-cycling, thereby greatly decreasing the computational requirements. If nonlinear errors along y are also considered as in (5.1), combining phase-cycling with low-resolution navigation would be an especially useful technique to reduce computation time.

Additionally, phase-cycling is compatible with parallel imaging techniques. The reconstruction method used in phase-cycling can be easily integrated with the SENSE algorithm [25], allowing iterative correction of motion artifacts in parallel multi-shot DWEPI images. The combination of phase-cycling with SENSE would enable

faster multi-shot DWEPI acquisition with inherent artifact correction, and would be beneficial in improving DWI efficiency.

6

Conclusion

The iterative phase estimation technique developed in this study has demonstrated the ability to correct motion-induced artifacts in multi-shot DWEPI without the use of navigators and the cost of longer scan times. Additionally, the method presented here has exhibited two key advantages over other iterative correction methods, namely a significant improvement in computation time, and a mathematical framework which can account for nonlinear errors.

Future studies can further evaluate the robustness of the technique. Possibilities include: assessment of the nonlinear phase-cycling model to correct nonlinear variations along the phase encoding direction, integration with 1D navigators to further reduce computation time, integration with parallel imaging, and extension of the method to eight-shot DWEPI.

Results of this study establish iterative phase-cycling as a novel and efficient method for correcting motion artifacts in diffusion-weighted imaging, thus making the presented technique highly pertinent for many high resolution DWI applications.

Appendix A

Review of MRI and DWI Principles

This chapter briefly reviews the basic physics and principles of magnetic resonance imaging (MRI), as well as the specific techniques and principles in diffusion-weighted MRI (DWI).

A.1 MR Physics

A.1.1 Nuclear Spins

All physical objects can be described by their constituent molecules, and furthermore by the atoms and nuclei within these molecules. The particles which comprise nuclei (protons, neutrons, and electrons) all have the property of *spin*, and each individual particle has a spin value of $\frac{1}{2}$. Because most spins are paired together, nuclei containing equal numbers of protons and neutrons will have an overall spin of zero. Only nuclei with odd numbers of protons and/or neutrons will have nonzero spin. The value of a nucleus' overall spin is known as the *spin quantum number (I)*.

Within the human body the most abundant nucleus is that of hydrogen, specifically the ^{1}H isotope, which contains one proton and no neutrons. Hydrogen nuclei

therefore have an overall spin of $I = \frac{1}{2}$. It is the abundance of hydrogen nuclei in the body and their spin that is exploited in MRI to produce images of tissue inside the body.

While spin is a process characterized by quantum mechanics, it can be described with classical mechanics as a physical rotation about an axis, as depicted in Fig. A.1. Nuclei with spin possess an angular momentum $\vec{J}$, which in turn generates an associated magnetic field/magnetic moment $\vec{u}$. The two are related by the equation

$$\vec{u} = \gamma \vec{J} \tag{A.1}$$

where γ is the gyromagnetic ratio, a physical constant which is dependent on the nucleus type. For ^{1}H, $\gamma = 2.675$ x 10^8 rad/s/T.

A.1.2 Magnetic Moments and Net Magnetization

Note that the magnetic moment $\vec{u}$ is a vector quantity, and therefore has both a magnitude and direction. In the absence of an external magnetic field the directions of nuclear magnetic moments are random, and as a result there is no net macroscopic magnetization in a collection of spins Fig. A.2a. However when an external magnetic field (of strength B_0) is applied, the magnetic moments align either parallel or anti-parallel with the external field, corresponding to low and high energy states, respectively (Fig. A.2b). Conventionally the external magnetic field $\vec{B_0}$ is applied

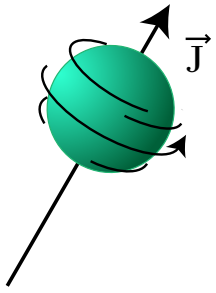

FIGURE A.1: Spin of a proton, characterized as a physical rotation about an axis and possessing an angular momentum $\vec{J}$

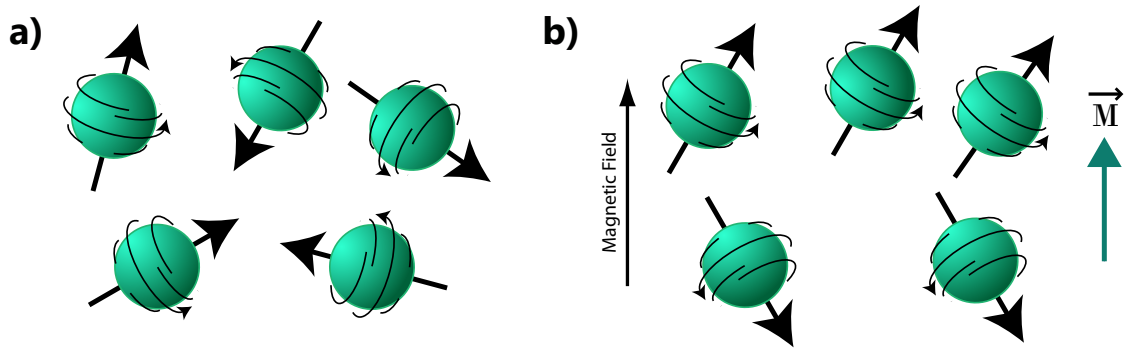

FIGURE A.2: **(a)** Randomly oriented spins in the absence of a magnetic field. **(b)** Alignment of spins in the presence of a magnetic field, resulting in a net magnetization $\vec{M}$.

along the z-direction. The magnitude of the magnetic moments in the presence of this field is then given by:

$$u_z = \gamma m_I \hbar \tag{A.2}$$

where $\hbar$ is Planck's constant (6.6 x10^{-34} J-s) divided by 2π, and m_I is the *magnetic quantum number*, which is related to the spin quantum number I. In the case of hydrogen, m_I takes on the values of $-I = -\frac{1}{2}$ and $+I = +\frac{1}{2}$. The energies E of the nuclei in the magnetic field can also be calculated according to quantum theory:

$$E = -\vec{u} \cdot \vec{B_0} = -u_z B_o = \gamma m_I \hbar B_0 \tag{A.3}$$

Therefore for spins in the low energy state (parallel with the magnetic field, $m = -\frac{1}{2}$),

$$E = -\frac{1}{2}\gamma \hbar B_0 \tag{A.4}$$

and for spins in the high energy state (anti-parallel with field, $m = +\frac{1}{2}$),

$$E = \frac{1}{2}\gamma \hbar B_0 \tag{A.5}$$

It can be derived through Boltzmann statistics that the total number of spins in the low energy state exceeds the number in the high energy state at equilibrium [26].

The result is a net macroscopic magnetization $\vec{M}$ in the direction of the external field (Fig. A.2b).

A.1.3 RF Excitation

In order to generate a measurable signal the net magnetization $\vec{M}$ generated by the external field $\vec{B}_0$ must be perturbed. An important property of spins within the external field is that they undergo a motion known as *nuclear precession* about the $\vec{B}_0$ axis (z-axis in our discussion). This motion is similar to the wobbling of a spinning top (Fig. A.3). The angular frequency at which the spins precess about z-axis is known as the *Larmor Frequency* and is given by:

$$\omega_0 = \gamma B_0 \tag{A.6}$$

Larmor frequencies are In order to perturb $\vec{M}$, and additional temporary magnetic field must be applied. This new magnetic field, known as the *excitation pulse* $\vec{B}_1(t)$ is a radio frequency (RF) pulse which must oscillate with a frequency equal to the Larmor frequencies of the nuclei. The result is that some of the spins originally in the low-energy state are promoted to the high-energy state. This causes a change, or

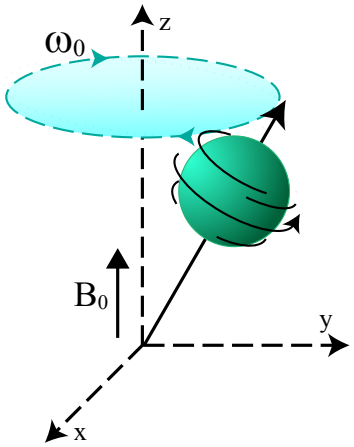

FIGURE A.3: **(a)** Randomly oriented spins in the absence of a magnetic field. **(b)** Alignment of spins in the presence of a magnetic field, resulting in a net magnetization $\vec{M}$.

"tipping" of the net magnetization $\vec{M}$. The amount by which $\vec{M}$ is tipped is known as the *flip angle*, and is a property of the shape of $\vec{B_1}(t)$. In this and subsequent discussions we assume a flip angle of 90°, i.e. $\vec{M}$ is tipped from the z-axis onto the xy-axis.

A.1.4 Relaxation

After excitation the $\vec{B_1}(t)$ pulse is subsequently turned off. At this point the spins begin to return to their equilibrium conditions through the process of *relaxation*. This process is observable through the change in the net magnetization $\vec{M}$. There are two types of relaxation processes: T_1, the longitudinal relaxation, and T_2, the transverse relaxation.

Longitudinal relaxation describes the recovery of the net magnetization onto the z-axis, and is characterized by the time constant T_1. Initially (after the application of the $\vec{B_1}(t)$ pulse), there is no z-component of $\vec{M}$. During relaxation the z-component recovers according to the equation

$$M_z(t) = M_0(1 - e^{-t/T_1}) \tag{A.7}$$

where M_0 is the magnitude of $\vec{M}$ during equilibrium before excitation.

Transverse relaxation describes the loss of the xy-component of $\vec{M}$ and is characterized by the time constant T_2. Initially $\vec{M}$ is entirely in the xy-plane. During relaxation the xy-component decays according to

$$M_{xy}(t) = M_0 e^{-t/T_2} \tag{A.8}$$

Different tissues within the body have different characteristic T_1 and T_2 values. By using a combination of excitation pulses, known as a pulse sequence, MRI signals can be made sensitive to these relaxation differences in order to create contrast among tissues in the final image. This is the basis of creating MR images.

A.1.5 Signal Detection

The generation of the $\vec{B_1}(t)$ pulse is done using a radio frequency coil. Typically the coil used to generate the pulse (known as the *transmit coil*) is the same used for subsequent signal detection (*receiver coil*). Signal detection is based on Faraday's law, which states that a time-varying magnetic flux through a conducting loop induces a current in the loop. In the case of MRI, the time-varying magnetic flux is net magnetization $\vec{M}$ during excitation and relaxation, and the conducting loop is the receiver coil. The current induced in the receiver coil during excitation/relaxation is the raw MR signal, *S(t)* which is later reconstructed into an image.

A.2 Image Formation

The previous section discussed the various physical principles involved to ultimately generate the raw MR signal. The following section describes the engineering principles behind forming an actual MR image.

A.2.1 Hardware

At this point it is important to include a brief discussion on the hardware used in an MR scanner.

Main Magnet

The main magnet produces the $\vec{B_0}$ field. In most modern scanners the main magnet is a large, cylindrical superconducting electromagnet capable of producing very strong magnetic fields. The stronger the magnetic field, the better the image resolution and signal-to-noise ratio [26]. Most clinical settings currently use scanners with a field strength of $|\vec{B_0}| = 3.0$ Teslas (T). To put this strength into perspective, note that that strength of the earth's magnetic field is approximately 5.0 x 10^{-5} T. Scanners

capable of producing even higher field strengths (7 - 12 T) are typically encountered in research settings.

Gradient System

As will be discussed in further detail later, an MR scanner incorporates three orthogonal (x,y,z) gradient coils capable of producing magnetic field gradients. These gradients enable signal localization by varying the overall magnetic field strength as a function of location within the scanner. Typical gradient strengths in scanners can range from 10 milliTesla per meter (mT/m) to 100 mT/m [27].

RF System

As mentioned in the previous section, a scanner contains RF coils which are used to generate and receive MR signals. The coil used to generate the signal via the $\vec{B_1}(t)$ pulse is known as the *transmit coil*, and the coil which detects the signal is the *receive coil*. Normally a single coil can be used as both the transmit and receive coil.

A.2.2 Signal Characteristics

Free Induction Decay

The signal after a single $\vec{B_1}(t)$ pulse decays as the net magnetization relaxes back to its equilibrium state. This is known as a free induction decay (FID) signal, the name coming from the net magnetization's *free* precession back to equilibrium after the RF pulse, and the process of *induction* used to receive the signal. Ideally the rate at which the FID signal decays would be dependent on the transverse relaxation T_2, resulting from random interactions among spins. However FID signals actually decay at a much faster rate, known as T_2^*. This is a result of imperfections in the system which result in a $\vec{B_0}$ field that is not perfectly homogeneous. An inhomogenous field where the strength varies slightly over space causes spins in different locations

to precess at different frequencies, leading to destructive interference in the overall signal. This faster observed decay is characterized by the T_2^* time constant.

Gradient Echoes

The rapidly decaying FID signal can be recovered through the use of certain techniques. The recovered signal is known as an *echo*, and can be generated either by using additional RF pulses, in which case it is known as a spin echo, or by applying a refocusing magnetic gradient, in which case it is known as gradient echo. Here we will describe only gradient echoes, as they are the basis of the EPI technique which this study is focused upon.

When a magnetic field gradient is applied (using one of the gradient coils discussed in the hardware section) spins in different positions precess at different frequencies. This can be described by a modified version of the Larmor frequency equation which includes the gradient field. Here we consider the case of a negative gradient in the x-direction:

$$\omega(x) = \gamma(B_0 - G_x x) = \omega_0 - \gamma G_x x \tag{A.9}$$

where ω_0 is the original Larmor frequency of a spin when only in the $\vec{B_0}$ field, and G_x is the strength of the magnetic field gradient in the x-direction. We can also calculate the acquired phase of spins along x at a time t during the application of the gradient:

$$\phi(x,t) = -\gamma G_x x t \tag{A.10}$$

It becomes apparent that since spins at different locations acquire different phases, when summed together there is destructive interference of the signal. This interference leads to an even faster decay than that of T_2^*, known as T_2^{**}. However, if a positive x-gradient is applied following the negative gradient, the spins will gradually rephase, resulting in a regrowth of the signal. Assuming the negative x-gradient

is turned off and the positive x-gradient turned on at time τ, the phase of spins over time is now given by

$$\phi(x,t) = -\gamma G_x x\tau + \gamma G_x x(t-\tau) \quad \text{for } t > \tau \tag{A.11}$$

In this equation when $t = 2\tau$ the positive and negative gradient terms cancel and $\phi(x,t) = 0$. This means the phase for all spins at all locations have rephased to zero, leading to a recovered, or "echo", signal. When this process is repeated several times it results in several echoes, known as a gradient-echo train. This technique is utilized in EPI, as will be discussed later.

A.2.3 Slice Selection

In order to generate a 2D image of a specific cross section, or *slice*, of the body, it is necessary to apply a short-term magnetic gradient in the z-direction during the $\vec{B_1}(t)$ pulse. Without a gradient all spins throughout the body will precess at the same frequency based on the $\vec{B_0}$ field and therefore will all be excited by the $\vec{B_1}(t)$ pulse. In this case it would not be possible to distinguish signals from different areas of the body, and a cross-sectional image could not be reconstructed. In order to localize the signal to only one cross-setional region of the body where an image is desired, a G_z gradient must be applied. The application of this gradient causes spins to precess at different frequencies as a function of z:

$$\omega(z) = \gamma(B_0 + G_z z) = \omega_0 + \gamma G_z z \tag{A.12}$$

As discussed earlier only spins with the same frequency as the oscillating $\vec{B_1}(t)$ pulse will be excited. Therefore by selecting an appropriate $\vec{B_1}(t)$ pulse with a frequency corresponding to the frequency of spins in the desired z-plane slice given by (A.12) it is possible to excite only those spins, and is the first step in creating a 2D image of the desired region.

A.2.4 Spatial Encoding

After the desired cross section in the body has been excited with slice selection it is necessary to distinguish the signals from spins within the cross section. This is done by spatially encoding the signal through two processes, *frequency encoding* and *phase encoding*.

Frequency Encoding

Frequency encoding uses the same principles of applying magnetic gradients to make the frequencies of spins a function of space. Assuming the gradient in this case is applied in the x-direction, the Larmor frequency of a column of spins at a position x within the excited slice is

$$\omega(x) = \gamma(B_0 + G_x x) = \omega_0 + \gamma G_x x \tag{A.13}$$

The MR signal is acquired during frequency encoding after slice selection and phase encoding (discussed in the next section). With frequency encoding alone, spins precessing at different frequencies along x make the total MR signal *S(t)* a summation of individual spin signals of different frequencies. The Fourier Transform can then be used to decompose the total acquired signal *S(t)* into its individual frequency components, which correspond to locations along x as given by (A.13). Therefore frequency encoding gives the first part of the spatial information needed to reconstruct a 2D image.

Phase Encoding

The other part of the spatial information comes from phase encoding the signal. If only frequency encoding were used the signal would only be dependent on x and would contain no spatial information about the y direction. Phase encoding is therefore done in the y-direction, and is accomplished by briefly applying a magnetic

gradient along y. While the y-gradient is on, rows of spins along y within the slice precess at frequencies given by:

$$\omega(y) = \gamma(B_0 + G_y y) = \omega_0 + \gamma G_y y \tag{A.14}$$

Note that at first this is precisely like frequency encoding. However the y-gradient G_y is soon turned off after a time T_{pe}, and the rows of spins return to precessing at the same frequency, but now with different phases accumulated while G_y was on:

$$\phi(y) = -\gamma G_y y T_p e \tag{A.15}$$

Phase encoding is done before frequency encoding and signal acquisition. Then during frequency encoding each spin within the slice will have a unique phase (varying along y) and frequency (varying along x) combination. Now the signal *S(t)* contains spatial information in both x and y directions, enabling a 2D image reconstruction.

In all MRI images there are multiple phase encoding "steps". The process of excitation/slice selection, phase encoding, and frequency encoding are repeated several times but with different strengths of the phase encoding gradient G_y. Slice selection and frequency encoding parameters stay the same for each repetition; only the phase encoding changes. Repeating data acquisition with different phase encoding steps allows for images with higher resolutions. This concept is better understood from a k-space perspective.

A.2.5 k-space

k-space is the spatial frequency domain of an image, obtained by taking the two-dimensional Fourier transform of the image. When an MR signal is acquired the data is stored in k-space. When k-space has been "filled", an MR image can be reconstructed by taking the inverse Fourier transform of k-space. Both frequency encoding and phase encoding can be visualized in the k-space domain.

Since data acquisition occurs during frequency encoding, the sampled data makes a trajectory along the x-axis (frequency encoding axis) of k-space. The exact position k_x in the trajectory at a time t during acquisition, assuming the starting point is the center of k-space ($k_x = 0, k_y = 0$), is given by:

$$k_x = \frac{1}{2\pi}\gamma G_x t \tag{A.16}$$

Hence the k-space trajectory during a frequency encoding gradient is a horizontal line. It is important to note that the actual acquired data is not continuous along this trajectory, but is sampled at discrete points (Fig. A.4).

In the previous section it was mentioned that multiple phase encoding steps are necessary to obtain a high quality image. From a k-space perspective this can be understood by realizing that images with high spatial resolution have a large amount of spatial frequency information. Therefore by sampling more spatial frequencies in k-space, a higher resolution image can be reconstructed. This is done by acquiring rows of horizontal lines in k-space by repeating frequency encoding numerous times. To do this, the starting y-position in k-space k_y must be changed with each repetition. This is the job of phase encoding before frequency encoding. After phase encoding

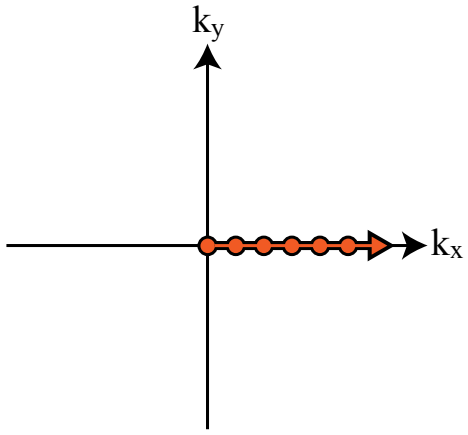

FIGURE A.4: Horizontal k-space trajectory (orange line) in frequency encoding. Data is sampled at discrete points along the trajectory (orange dots).

the starting vertical position k_y is given by:

$$k_y = \frac{1}{2\pi}\gamma G_y T_{pe} \tag{A.17}$$

where T_{pe} is the duration of phase encoding.

Following phase encoding, frequency encoding/acquisition is performed to acquire a horizontal line in k-space. It can be seen from (A.17) that by changing the strength of G_y the starting y-position k_y can be changed. Therefore for each repetition G_y is changed during phase encoding to start at a new k_y position, allowing a new horizontal line to be acquired. The more times this process is repeated, the more k-space is covered, leading to data with more spatial frequency information and therefore a reconstructed image with greater spatial resolution. The entire process, including the changes in G_y for each repetition, is depicted in Fig. A.5 in what is known as a pulse-sequence diagram.

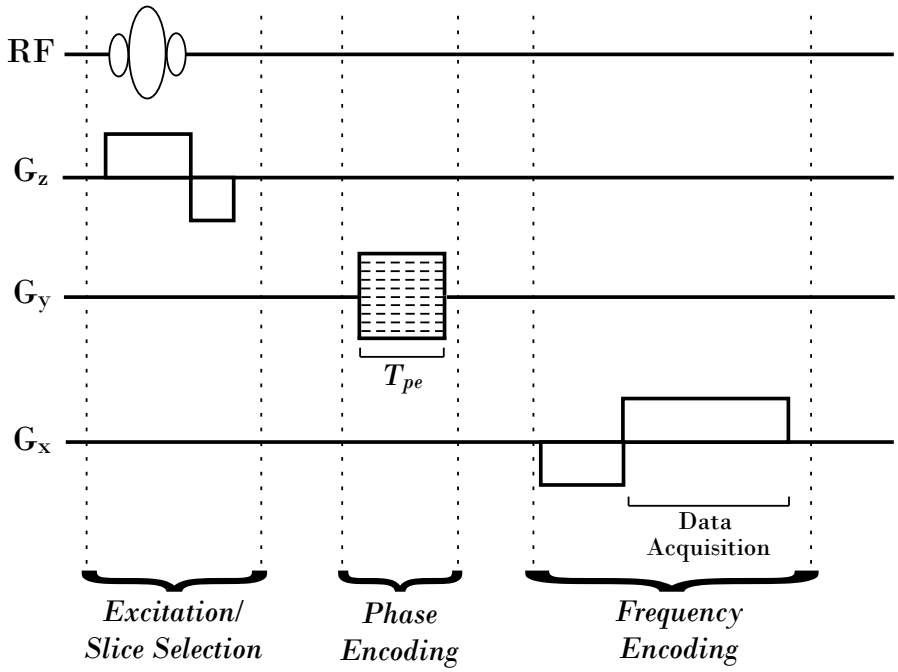

FIGURE A.5: A pulse sequence which is repeated several times with different phase encoding strengths (dashed lines) to acquire multiple rows of k-space.

As mentioned earlier, the data along each horizontal trajectory is not continuous, but sampled at discrete points. The number of sampled points along each line is typically equal to the number of total lines acquired, i.e. the total data is a square matrix. As an example, a pulse sequence that acquires 64 lines will sample 64 points along each line, resulting in a k-space data matrix of 64x64.

A.2.6 Echo-Planar Imaging

Echo-Planar Imaging (EPI) is a pulse sequence widely used in practice due to its very fast imaging speed [20, 26, 28]. Many lines (commonly between 64-128 lines) of k-space can be acquired with just one RF excitation. This is done by using rapidly switched gradients during excitation. See Fig. A.6. The small phase encoding "blips" between each frequency encoding gradient changes the starting k_y position of each acquired line. Thus several rows of horizontal k-space lines are acquired after just one excitation. This is in contrast to the pulse sequence diagram shown in Fig. A.5, where several excitations are used and the phase encoding gradient changes with each repetition. The k-space trajectory/data of an EPI sequence is shown in Fig. A.7.

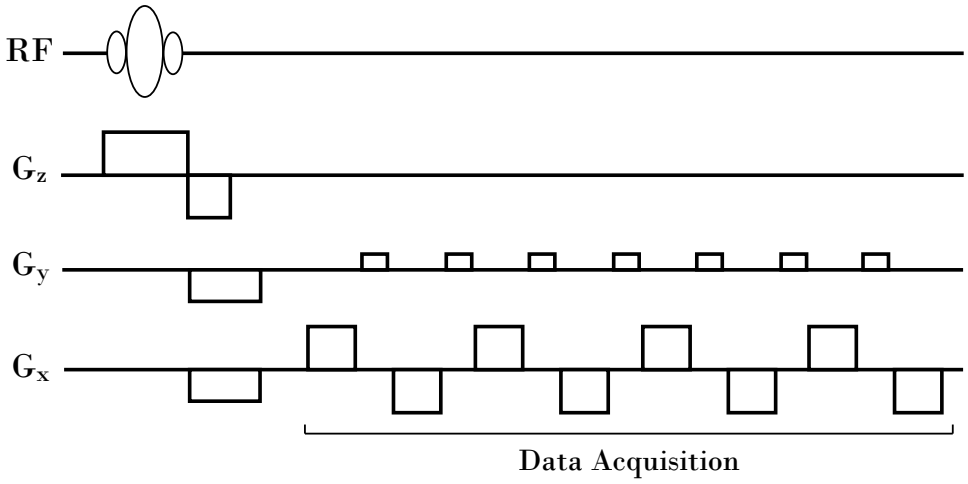

FIGURE A.6: EPI pulse sequence using rapidly switched gradients to acquire k-space in a single RF excitation

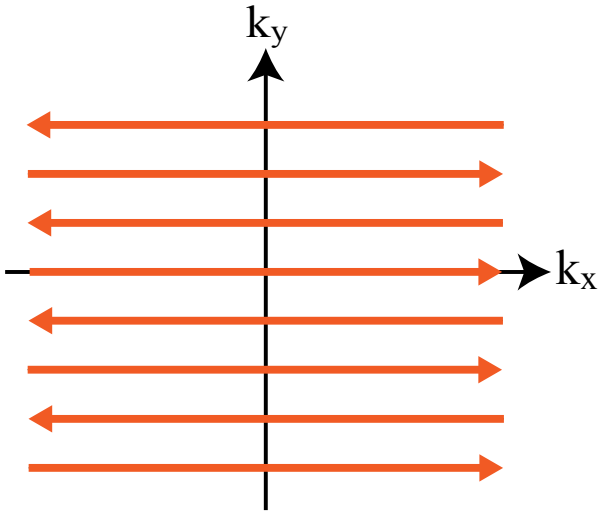

FIGURE A.7: Acquired k-space trajectories for an EPI sequence.

As discussed before, the decay of a signal from a single excitation is characterized by the T_2^* time constant, which is typically on the order of 60 ms. Because only one excitation pulse is used for acquiring data in EPI, the gradients must be applied very rapidly in order to sample enough of k-space before the signal decays completely. This results in a very fast sequence and hence a very short scan time, which is an important advantage of EPI and is why it used so often clinically.

A.2.7 Multi-Shot Echo-Planar Imaging

The EPI method described above is often referred to as *single-shot* EPI (ss-EPI) because all of k-space is acquired in only one excitation, or "shot". While ss-EPI's main advantage is reduced scan-time, it suffers from several limitations including low signal-to-noise ratio (SNR), vulnerability to image distortions (or *artifacts*), and limited attainable spatial-resolution due to the fast signal decay [4, 14, 27]. In order to overcome these limitations, *multi-shot* EPI (ms-EPI) can be used.

Multi-shot EPI follows the same principles as ss-EPI except it uses multiple excitations to acquire k-space data. One way to acquire the data is in an interleaved manner, where the acquired lines of each shot fill in the gaps from the other shots. As

an example, assuming 64 lines of k-space were desired, in two-shot EPI only 32 lines would be acquired for each excitation. In an interleaved acquisition the first shot would acquire lines 1,3,5,7, etc. while the second shot would acquire lines 2,4,6,8, etc. Therefore each shot traverses the y-direction of k-space much faster than in ss-EPI, and this results in reduced distortions that occur in ss-EPI due to its slow k_y sampling rate [4].

While the example above involved only 64 lines of k-space, one of ms-EPI's main advantages is its ability to acquire a much greater number of k-space lines. In ss-EPI the total number of attainable lines is limited because of the T_2^* signal decay of a single excitation. In ms-EPI the number of lines in each shot is also limited by T_2^* decay, but by combining data from each shot the total amount of lines is increased, and is limited only by the number of excitations used. This results in a larger k-space coverage and therefore improved spatial resolution. Additionally, since in ms-EPI the number of k-space lines acquired in each shot is not stretched to the maximum as in ss-EPI, the acquired signal from each shot does not decay as much as much as in ss-EPI, resulting in better SNR.

The number of shots commonly used in practice are currently two, four, and eight, with two/four-shot EPI being the most typical. Typical sizes of acquired k-space data in ms-EPI are 256x256 or greater, whereas sizes typical of ss-EPI range from 64x64 to 128x128 [20].

A.3 Diffusion-Weighted Imaging

Water molecules within the body move by diffusion, specifically according to a process known as Brownian Motion [20, 27]. Molecules can either diffuse freely in all directions, known as isotropic diffusion, or can be restricted to only certain directions, known as anisotropic diffusion. In the body water molecules are restricted by cell membranes and tissue structure, and therefore are characterized by anisotropic

diffusion.

The ability of molecules to diffuse in the brain varies among different regions due to variations in brain tissue structure. This variation of diffusion can be exploited by MRI to create contrast in images, thereby providing great detail of brain structure. The technique is known as Diffusion-Weighted Imaging (DWI). DWI involves the use of two large gradient pulses, referred to as diffusion gradients, applied before a typical acquisition sequence such as ss-EPI or ms-EPI. The ability of these diffusion gradients to create diffusion weighted contrast is easily understood when the principles of a gradient echo are considered.

The first diffusion gradient is a large positive gradient, and the second is a large negative gradient of equal magnitude and length of the first. This is the exact same process used to formed gradient echoes, as described in Section A.2.2. Just as in the formation of gradient echoes, at the end of second diffusion gradient all spins dephased from the first diffusion gradient should become rephased. However because the diffusion gradients are of a much greater strength (40 - 80 mT/m) than the gradients used for gradient echoes, the signal becomes very sensitive to motion of the spins. Spins which are stationary or do not move very much become completely or mostly rephased after the second gradient. However spins which are moving do not become totally rephased.

The stationary spins correspond to water molecules in brain tissue with slow diffusion properties, while the moving spins correspond to molecules in brain tissue with fast diffusion. Because the moving spins in tissue with fast diffusion are not rephased completely, the acquired signal in these regions is attenuated. Therefore when the final image is reconstructed, tissue with fast diffusion appears darker than tissue with slow diffusion. This is the diffusion-weighted contrast.

Fig. A.8 shows the beginning of a DWI sequence where the diffusion gradients are applied. Following the diffusion gradients is a standard pulse sequence to acquire

the actual image data. Although any pulse sequence can be used, ss-EPI or ms-EPI are typically used due to their advantages mentioned above.

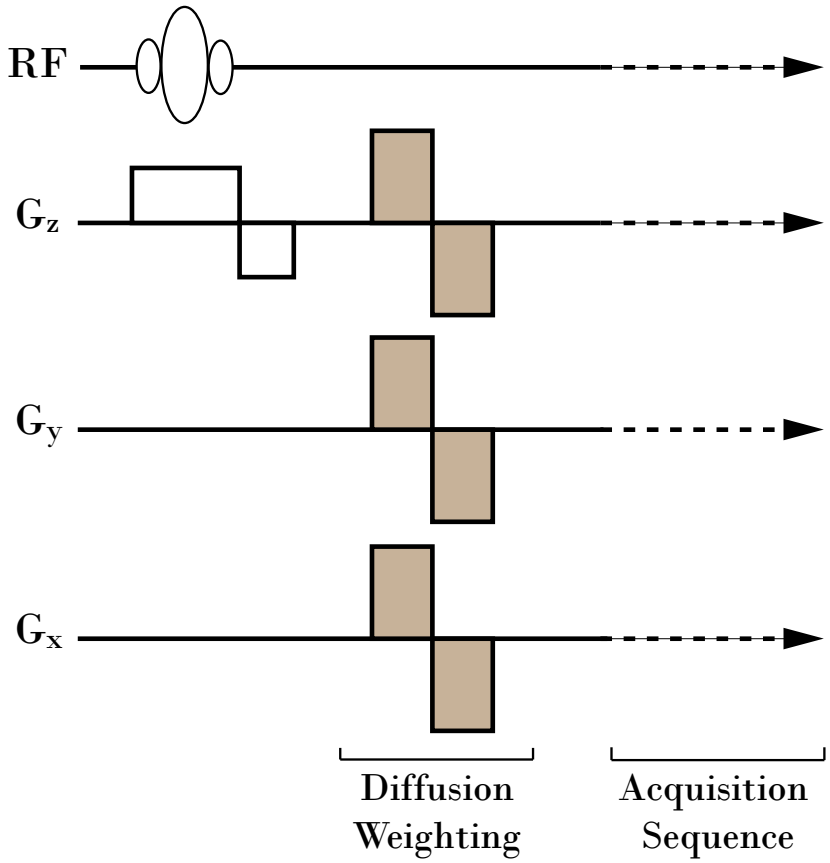

FIGURE A.8: Diffusion gradients (in gray) applied in all gradient directions at the beginning of a pulse sequence. Note the gradient sizes are not to scale; diffusion gradients are typically much stronger than slice selection or acquisition gradients.

Bibliography

[1] M. E. Moseley *et al.*, "Diffusion-weighted MR imaging of acute stroke: correlation with T2-weighted and magnetic susceptibility-enhanced MR imaging in cats," *American Journal of Neuroradiology*, vol. 11, pp. 423–429, 1990.

[2] S. Warach, D. Chien, W. Li, M. Ronthal, and R. Edelman, "Fast magnetic resonance diffusion-weighted imaging of acute human stroke," *Neurology*, vol. 42, pp. 1717–1723, 1992.

[3] M. G. Lansberg *et al.*, "Advantages of Adding Diffusion-Weighted Magnetic Resonance Imaging to Conventional Magnetic Resonance Imaging for Evaluating Acute Stroke," *Archives of Neurology*, vol. 57, pp. 1311–1316, 2000.

[4] R. Bammer, "Basic principles of diffusion-weighted imaging," *European Journal of Radiology*, vol. 25, pp. 169–184, 2003.

[5] T. Ebisu *et al.*, "Discrimination of brain abscess from necrotic or cystic tumors by diffusion-weighted echo planar imaging," *Magnetic Resonance Imaging*, vol. 14, pp. 1113–1116, 1996.

[6] P. H. Lai, "Brain Abscess and Necrotic Brain Tumor: Discrimination with Proton MR Spectroscopy and Diffusion-Weighted Imaging," *American Journal of Neuroradiology*, vol. 23, pp. 1369–1377, 2002.

[7] S. Mori, B. J. Crain, V. Chacko, and P. C. M. van Zijl, "Three-Dimensional Tracking of Axonal Projections in the Brain by Magnetic Resonance Imaging," *Annals of Neurology*, vol. 45, pp. 265–269, 1999.

[8] P. J. Basser, S. Pajevic, C. Pierpaoli, J. Duda, and A. Aldroubi, "In Vivo Fiber Tractography Using DT-MRI Data," *Magnetic Resonance in Medicine*, vol. 44, pp. 625–632, 2000.

[9] O. Ciccarelli, M. Catani, H. Johansen-Berg, C. Clark, and A. Thompson, "Diffusion-based tractography in neurological disorders: concepts, applications, and future developments," *The Lancet Neurology*, vol. 7, pp. 715–727, 2008.

[10] T. Moritani, S. Ekholm, and P.-L. Westesson, *Diffusion-Weighted MR Imaging of the Brain*, 2nd ed. Berlin: Springer-Verlag, 2009.

[11] K. Butts, A. de Crespigny, J. M. Pauly, and M. Moseley, "Diffusion-Weighted Interleaved Echo-Planar Imaging with a Pair of Orthogonal Navigator Echoes," *Magnetic Resonance in Medicine*, vol. 35, pp. 763–770, 1996.

[12] K. L. Miller and J. M. Pauly, "Nonlinear Phase Correction for Navigated Diffuson Imaging," *Magnetic Resonance in Medicine*, vol. 50, pp. 343–353, 2003.

[13] C. Liu, R. Bammer, D. hyun Kim, and M. E. Moseley, "Self-Navigated Interleaved Spiral (SNAILS): Application to High-Resolution Diffusion Tensor Imaging," *Magnetic Resonance in Medicine*, vol. 52, pp. 1388–1396, 2004.

[14] A. T. Van, D. C. Karampinos, J. G. Georgiadis, and B. P. Sutton, "K-space and Image-Space Combination for Motion-Induced Phase-Error Correction in Self-Navigated Multicoil Multishot DWI," *IEEE Transactions on Medical Imaging*, vol. 28, no. 11, pp. 1770–1780, 2009.

[15] A. J. de Crespigny, M. P. Marks, D. R. Enzmann, and M. E. Moseley, "Navigated Diffusion Imaging of Normal and Ischemic Human Brain," *Magnetic Resonance in Medicine*, vol. 33, pp. 720–728, 1995.

[16] K. Butts, J. Pauly, A. de Crespigny, and M. Moseley, "Isotropic Diffusion-Weighted and Spiral-Navigated Interleaved EPI for Routine Imaging of Acute Stroke," *Magnetic Resonance in Medicine*, vol. 38, pp. 741–749, 1997.

[17] D. Atkinson, D. A. Porter, D. L. Hill, F. Calamante, and A. Connelly, "Sampling and Reconstruction Effects Due to Motion in Diffusion-Weighted Interleaved Echo Planar Imaging," *Magnetic Resonance in Medicine*, vol. 44, pp. 101–109, 2000.

[18] T.-Q. Li, D.-H. Kim, and M. E. Moseley, "High-Resolution Diffusion-Weighted Imaging With Interleaved Variable-Density Spiral Acquisitions," *Journal of Magnetic Resonance Imaging*, vol. 21, pp. 468–475, 2005.

[19] D. Atkinson *et al.*, "Nonlinear Phase Correction of Navigated Multi-coil Diffusion Images," *Magnetic Resonance in Medicine*, vol. 56, pp. 1135–1139, 2006.

[20] M. A. Bernstein, K. F. King, and X. J. Zhou, *Handbook of MRI Pulse Sequences*. Elsevier Academic Press, 2004.

[21] A. W. Anderson and J. C. Gore, "Analysis and Correction of Motion Artifacts in Diffusion Weighted Imaging," *Magnetic Resonance in Medicine*, vol. 32, pp. 379–387, 1994.

[22] M. D. Robson, A. W. Anderson, and J. C. Gore, "Diffusion-Weighted Multiple Shot Echo Planar Imaging of Humans without Navigation," *Magnetic Resonance in Medicine*, vol. 38, pp. 82–88, 1997.

[23] R. G. Nunes, P. Jezzard, T. E. J. Behrens, and S. Clare, "Self-Navigated Multi-shot Echo-Planar Pulse Sequence for High-Resolution Diffusion-Weighted Imaging," *Magnetic Resonance in Medicine*, vol. 53, pp. 1474–1478, 2005.

[24] C. Liu, M. E. Moseley, and R. Bammer, "Simultaneous Phase Correction and SENSE Reconstruction for Navigated Multi-Shot DWI with Non-Cartesian k-Space Sampling," *Magnetic Resonance in Medicine*, vol. 54, pp. 1412–1422, 2005.

[25] N.-K. Chen, A. V. Avram, and A. W. Song, "Two-Dimensional Phase Cycled Reconstruction for Inherent Correction of Echo-Planar Imaging Nyquist Artifacts," *Magnetic Resonance in Medicine*, vol. 66, pp. 1057–1066, 2011.

[26] Z.-P. Liang and P. C. Latuerbur, *Principles of Magnetic Resonance Imaging: A Signal Processing Perspective*. New York, NY: IEEE Press, 2000.

[27] D. W. McRobbie, E. A. Moore, M. J. Graves, and M. R. Prince, *MRI: From Picture to Proton*, 2nd ed. New York, NY: Cambridge University Press, 2006.

[28] S. Skare *et al.*, "Clinical Multishot DW-EPI Through Parallel Imaging With Considerations of Susceptibility, Motion, and Noise," *Magnetic Resonance in Medicine*, vol. 57, pp. 881–890, 2007.